



Research Repository UCD

Title	Flow Induced Crystallization of Poly(ether-block-amide) from the Microinjection Molding Process and its Effect on Mechanical Properties
Authors(s)	Zhang, Nan, Choi, Seong Ying, Gilchrist, M. D.
Publication date	2014-11
Publication information	Zhang, Nan, Seong Ying Choi, and M. D. Gilchrist. "Flow Induced Crystallization of Poly(Ether-Block-Amide) from the Microinjection Molding Process and Its Effect on Mechanical Properties." Wiley Blackwell (John Wiley & Sons), November 2014. https://doi.org/10.1002/mame.201300459 .
Publisher	Wiley Blackwell (John Wiley & Sons)
Item record/more information	http://hdl.handle.net/10197/5942
Publisher's statement	This is the author's version of the following article: Nan Zhang, Seong Ying Choi, & Michael D. Gilchrist (2014) "Flow Induced Crystallization of Poly(ether-block-amide) from the Microinjection Molding Process and its Effect on Mechanical Properties" Macromolecular Materials and Engineering: 299(11) which has been published in final form at http://dx.doi.org/10.1002/mame.201300459 .
Publisher's version (DOI)	10.1002/mame.201300459

Downloaded 2025-12-04 23:03:38

The UCD community has made this article openly available. Please share how this access benefits you. Your story matters! (@ucd_oa)



© Some rights reserved. For more information

Macromolecular Materials and Engineering

Flow induced crystallization of Poly(ether-block-amide) from the microinjection molding process and its effect on mechanical properties --Manuscript Draft--

Manuscript Number:	name.201300459R1		
Full Title:	Flow induced crystallization of Poly(ether-block-amide) from the microinjection molding process and its effect on mechanical properties		
Article Type:	Full Paper		
Keywords:	shear induced crystallization; short-term shear protocol; spherulite-free core structure; critical shear stress; specific work		
Corresponding Author:	Michael D. Gilchrist, Prof. University College Dublin Dublin 4, Please Select IRELAND		
Corresponding Author Secondary Information:			
Corresponding Author's Institution:	University College Dublin		
Corresponding Author's Secondary Institution:			
First Author:	Nan Zhang, PhD		
First Author Secondary Information:			
Order of Authors:	Nan Zhang, PhD		
	Seong Ying Choi, PhD		
	Michael D. Gilchrist, Prof.		
Order of Authors Secondary Information:			
Abstract:	<p>Crystallization of Poly(ether-block-amide) during microinjection molding is investigated using polarized light microscopy, atomic force microscopy, small/wide angle X-ray scattering and differential scanning calorimetry. Special morphologies of micro dumbbell parts, such as spherulitic or spherulite-free core structures and unique spherulite structures generated beneath the skin layers, are examined and explained relative to processing conditions. Nanoindentation tests confirm that both the modulus and hardness of the skin layer are higher than the core layer, regardless of the core structure. Uniaxial tensile testing indicates that Young's modulus, strain at break and yield stress all increase with an increase of skin ratio. The relationship between process, morphology and mechanical properties are systematically studied for micro products. Additionally, by using in-line process monitoring, flow induced crystallization of polymer filling of a dumbbell part is characterized by shear stress and apparent specific work. By comparison with a "short-term shear protocol", shear stress is validated to be a good candidate to characterize the formation of highly oriented structures under an actual microinjection molding process. This may provide a method for in-line control of morphology development and then final properties by controlling the flow conditions.</p>		
Additional Information:			
Question	Response		
<p>Please submit a plain text version of your cover letter here.</p> <p>Please note, if you are submitting a revision of your manuscript, there is an opportunity for you to provide your responses to the reviewers later; please do not add them to the cover letter.</p>	<p>Dear Editor,</p> <p>Please find attached extensively revised manuscript that addresses all of the reviewers criticisms and queries, along with Support Material.</p> <p>I trust that you will consider this suitable for full review and ultimately for publication in the journal and look forward to hearing from you in due course.</p>		

	<p>Yours faithfully,</p>
--	--------------------------

	<p>Michael Gilchrist</p>
--	--------------------------

Full Paper

Flow induced crystallization of Poly(ether-block-amide) from the microinjection molding process and its effect on mechanical properties^a

Nan Zhang¹, SeongYing Choi¹, *Michael D. Gilchrist¹

¹School of Mechanical and Materials Engineering, University College Dublin, Ireland

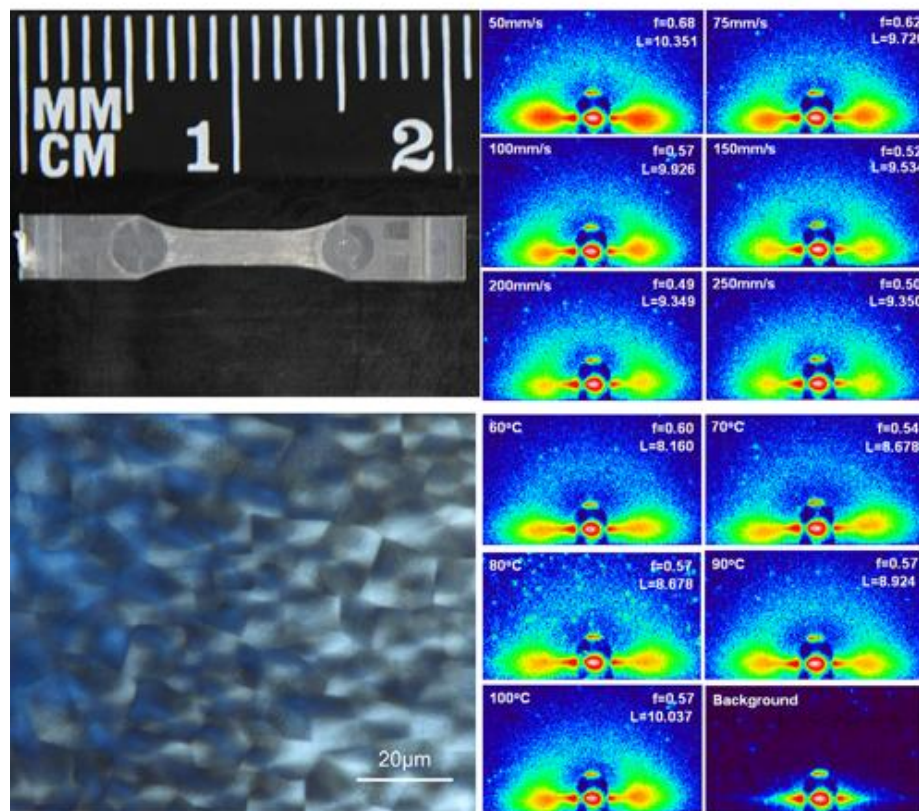
***Corresponding Author: Michael Gilchrist**

Email: michael.gilchrist@ucd.ie

ABSTRACT. Crystallization of Poly(ether-block-amide) during microinjection molding is investigated using polarized light microscopy, atomic force microscopy, small/wide angle X-ray scattering and differential scanning calorimetry. Special morphologies of micro dumbbell parts, such as spherulitic or spherulite-free core structures and unique spherulite structures generated beneath the skin layers, are examined and explained relative to processing conditions. Nanoindentation tests confirm that both the modulus and hardness of the skin layer are higher than the core layer, regardless of the core structure. Uniaxial tensile testing indicates that Young's modulus, strain at break and yield stress all increase with an increase of skin ratio. The relationship between process, morphology and mechanical properties are systematically studied for micro products. Additionally, by using in-line process monitoring, flow induced crystallization of polymer filling of dumbbell part is characterized by shear stress and apparent specific work. By comparison with a "short-term shear protocol", shear stress is validated to be a good candidate to characterize the formation of highly oriented

^a **Supporting Information** is available online from the Wiley Online Library or from the author

structures under actual microinjection molding process. This may provide a method for in-line control of morphology development and then final properties by controlling the flow conditions.



1. Introduction

1.1 Flow induced crystallization

Crystallization of semicrystalline polymers depends highly on molecular structure and processing conditions. Such processing involves high pressures, high shear rates and high cooling rates etc., and this influences the crystallization kinetics and results in the formation of either highly oriented structures or random spherulitic crystals. The relative proportions of these two structures are one of the main factors that influence the optical, thermal, transport and mechanical properties of commercial products^[1]. Flow is found to be the only reason for the formation of highly oriented structures. Research in recent years on shear-induced crystallization has sought to identify the boundary flow conditions for the onset of an oriented morphology, described by shear stress, shear rate, shear strain, specific work or combinations of these^[1-7]. However, it is still unknown how best to define such thresholds and whether such thresholds can be applied under real processing conditions^[8].

In an industrial production process, such as injection molding or extrusion, polymer materials are subject to combination of intense shear and heat transfer, which further complicates the crystallization process. Janeschitz-Kriegl and co-workers developed a “short-term shear protocol” by separating the influence of flow and temperature in order to study shear induced crystallization^[4]. This protocol has been used subsequently by many researchers^[1, 4, 6, 9-12]. In a short-term shear protocol, shear can be introduced by a piston with a weighted lever^[4], a pneumatic actuator^[9] or a high torque stepper motor^[7] etc., all of which control shear action and shear time. As shown in Figure 1 (a), the material is first heated up to a temperature above its equilibrium melting temperature (T_{mo}) and is maintained at this temperature for a period of time, t_{relax} , which is longer than the reptation time of the longest molecules, in order to erase all thermomechanical history. The shear pulse is then applied by an actuator, after the melt is cooled down to the target crystallization temperature,

which is above the melting temperature of spherulite crystals (T_{mc}) to eliminate temperature-driven nucleation ^[1, 13]. The shear time can be tens of seconds and shear stress is usually less than 100kPa, despite so-called “high stress” conditions ^[14, 15]. The corresponding shear rate is less than $100s^{-1}$ in order to sustain the measurement resolution at the boundary conditions ^[1]. Very slow cooling is then applied to crystallize the polymer melts. It was found that quench conditions and specific work can dramatically promote nucleation density by several orders of magnitudes ^[6]. Mykhaylyk et al. found that critical specific work and critical shear rate were effective thresholds for the formation of oriented structures based on a short-term shear protocol using a commercial parallel disc rheometer ^[1, 7]. Kornfield and colleagues used shear stress as a threshold to explain the onset of oriented structures under pressure driven flow using a short term shear protocol ^[2, 3, 8, 9]. For a given material, the formation of “point-like nuclei” starts once shear stress exceeds a threshold stress (σ_{pt}), below which the effect of shearing is negligible. “Point-like nuclei” can be transformed into “thread-like nuclei” where shear stress (σ) becomes higher than a critical shear stress ($\sigma_{critical}$). Nuclei that exist at the moment when shear stops govern morphology growth under quiescent-like conditions. Spherulite morphologies grow from “point-like” precursors, while orientated lamellae (known as “kebabs”) can grow from the nucleating surface of “thread-like” precursors (known as “shishes”). When “thread-like” nuclei become denser, cylindrilites impinge prior to significant noncrystallographic branching and a highly oriented morphology forms. Currently, studies of flow conditions on the onset of oriented structures are mainly based on using laboratory plate-plate rheometer ^[1], sliding plate rheometer ^[16] or customized pressure driven flow cell ^[2, 3, 8, 9]; very few attempts have been made to study or validate such thresholds under non-isothermal industrial processing conditions ^[17].

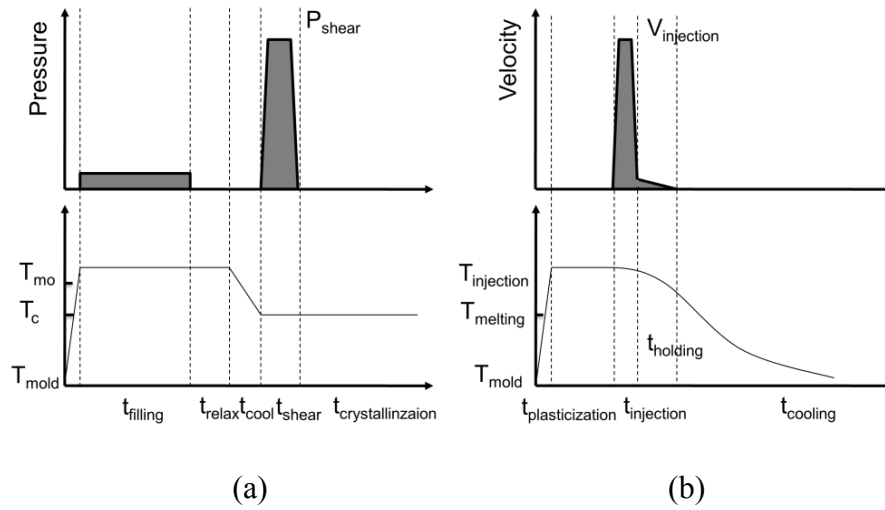


Figure 1. Schematic of short-term shear protocol (a) and injection molding process (b).

1.2 Microinjection molding

Microinjection molding is an extreme version of conventional injection molding. It produces polymer micro components or parts with micro/nano-scale features, such as microneedles, microgears and microfluidic chips ^[18]. Such products share a common feature of high surface to volume ratios (up to $10^3 \sim 10^6 \text{ m}^{-1}$) that can cause early solidification of polymer melts, leading to short shot defects. Therefore, a high injection pressure and a high mold temperature are generally used in the molding process. The polymer materials in microinjection molding are consequently subject to shear rates and thermal gradients much higher than in conventional injection molding. Higher thermal gradients result in a higher skin ratio, while high shear rates create highly oriented structures. However, a “skin-core” morphology is still maintained for most thermoplastic microinjection molded products when a part is thicker than $300\mu\text{m}$ ^[19-24], as discovered in conventional injection molding. When the part thickness is as small as $150\mu\text{m}$ or less, the oriented skin extends to the core region and results in a “core-free” morphology ^[21, 25], due to the high shear rate and fast cooling speed. However, such process/size-induced morphology has not been correctly correlated for miniature products. For example, there is no uniform correlation between the geometry of microinjection molded tensile bars and the changes of the mechanical properties, although the correlations between

the mechanical behavior and the testing parameters (temperature, strain rate) at the macro range are qualitatively valid for the micro range in most cases ^[26]. A systematic study of the relationship between process-morphology-properties of microinjection molded products is still rare.

Additionally, injection molding can also be treated as a short shear process under non-isothermal conditions. As shown in Figure 1 (b), polymer pellets are firstly sheared, compressed, melted and accumulated in front of an injection nozzle during the plasticization at a temperature which is usually above T_{mo} . The shear pulse is controlled by injection velocity, implemented by a server motor during the injection process, following the holding stage to fill more material into the cavity to compensate for shrinkage caused by solidification. The cooling process then follows and the entire part crystallizes until it is hard enough to be safely ejected out of the mold without damage. In contrast to a short shear protocol, injection molding involves both flow and heat transfer; thermo-mechanical histories from previous processes (plasticization, filling of sprue, runner and gate) are not erased in the injection molding process; cooling rate varies from skin to core because of high quench conditions; shear stress in a microinjection molding process can reach 0.6MPa with shear rate as high as $10^3 \sim 10^7 s^{-1}$ and shear time during filling lasts for tens of milliseconds based on in line process monitoring ^[27, 28]; these are around 1, 3 and 1~4 orders of magnitudes higher than in a short-term shear protocol, respectively.

1.3 Poly(ether block amide)

Poly(ether block amide), commercially known as Pebax[®], is a segmented block thermoplastic elastomer ^[29]. Medical grade Pebax is used in interventional medical devices, such as angiography, angioplasty and urology catheters, due to the wide range of physical and mechanical properties that can be achieved by varying the monomer block types and ratios ^[30, 31]. Some typical micro components molded with Pebax, such as catheter sheaths and catheter tips, have dimensions in the micrometer scale ^[32]. Most available Pebax studies to date

1 focused on film chemical composition on their microphase separation morphology and related
2 properties [29, 33-35]. Very few studies are available on the process-morphology of Pebax under
3
4 real processing conditions, such as injection molding [31].
5
6

7 **1.4 Motivation**

8
9
10 As discussed above, the present work has attempted to study the effect of extreme processing
11 on morphology and mechanical properties of Pebax in microinjection molding process.
12
13 Special morphologies of Pebax, such as spherulite-free core structures, irregular structures
14
15 between skin and core, were to be examined and explained. Nanoindentation and uniaxial
16
17 tensile testing were used to study local and bulk mechanical properties. The relationship of
18
19 process, morphological features (crystallinity, molecular orientation, long period and skin
20
21 ratio) and mechanical properties (Young's modulus, strain at break, yield stress and yield
22
23 strain) of micro parts were systematically studied using statistical analysis. Additionally, by
24
25 using in-line process monitoring, flow induced crystallization under a real microinjection
26
27 molding process was investigated by comparing it with a "short-term shear protocol".
28
29 Thresholds proposed in a laboratory-based "short-term shear protocol" were transferred to a
30
31 high stress, fast injection and non-isothermal real molding process. A careful comparison was
32
33 conducted to explore the possibility of using in-line process control to govern product
34
35 morphology and even its final properties.
36
37
38
39
40
41
42
43

44 **2. Materials and Methods**

45 **2.1 In-line process monitoring**

46
47
48 The rheological behavior of polymer melts was monitored with an insert mold utilizing a
49
50 reciprocating micro injection molding machine, Fanuc Roboshot S-2000i 15B, which is
51
52 equipped with a 14mm diameter injection screw. We designed a dumbbell mold cavity insert
53
54 to form the cavity with a depth of 400μm, as shown in Figures 2 (a) and (b). Two Kistler
55
56 6189A combined pressure and temperature sensors (PT sensors) with tip diameters of 2.5mm
57
58
59
60
61
62
63
64
65

were fitted into the waited region of the dumbbell mold cavity to directly detect the melt temperature and cavity pressure at the same position, as shown in Figure 2 (c). A Kistler CoMo injection process monitoring system (2869B) was used for data acquisition. The injection signals from the injection molding machine triggered the CoMo data acquisition system to ensure that all the signals were received simultaneously.

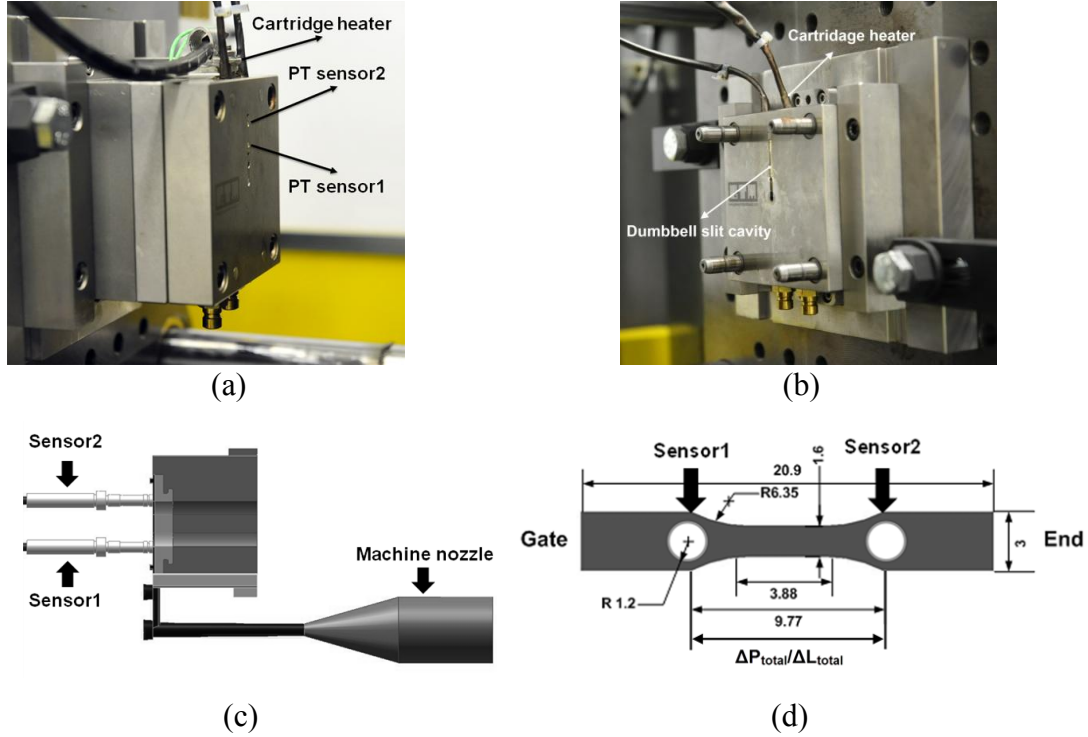


Figure 2. Mold and measurement system: (a) moving half, (b) stationary half, (c) pressure and temperature sensors, (d) micro molded dumbbell part.

Based on the slit flow model, shear rate and shear stress can be calculated by monitoring the amount of polymer exiting the slit die per unit time (Q) for a given pressure drop (ΔP)^[36]. The apparent shear rate and real shear stress are given by

$$\dot{\gamma}_{w(app)} = \frac{6Q}{wh^2} \quad (1)$$

where Q is volume flow rate and w , h are channel width and depth. The shear stress is given:

$$\tau_{w(real)} = \frac{h}{2} \left(\frac{-\Delta P}{L} \right) \quad (2)$$

where L is channel length. For our case, the ratio of length to depth is 24. Therefore, we believe that the entrance and exit waist regions would actually have a negligible effect on

pressure drop. The pressure gradient can be approximated by $\Delta P_{\text{total}}/\Delta L_{\text{total}}$, as shown in Figure 2 (d).

When the ratio of w/h of a rectangular channel is less than 10, the edge effect on the shear stress must be considered and the wall shear stress for Newtonian fluids is given by ^[37],

$$\tau_{w(\text{real})} = \frac{w \cdot h}{2(w+h)} \left(\frac{-\Delta P}{L} \right) \quad (3)$$

Figure 3 shows the typical trace curves of cavity pressure during 0.08s. It can be observed that the melt front reaches sensor 1 near the gate and travels to sensor 2 during time Δt_1 and the pressure drop is uniform during Δt_2 when the melt front reaches the part's end. The average pressure drop during Δt_2 was used to estimate the pressure gradient. The actual volume flow rate Q can be estimated by the actual volume of the dumbbell part between sensor 1 and sensor 2 over the time Δt_1 when the melts travels this corresponding distance. Thermomechanical history during plasticization is kept consistent for all processing conditions. More details on process monitoring and characterization can be found in our previous work ^[28, 38].

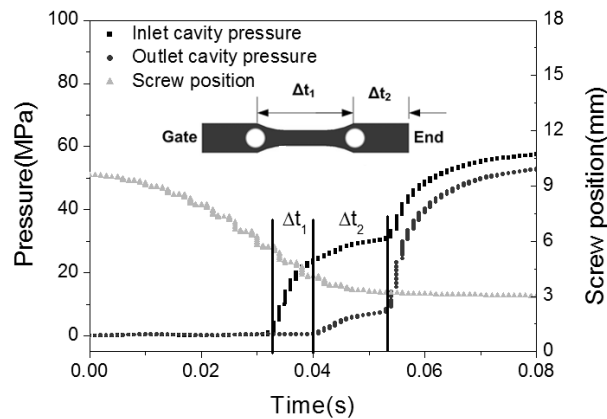


Figure 3. Typical cavity pressure and injection screw position during flow in the dumbbell die.

2.2 Materials

Pebax 7233 SA01 (Melt Mass Flow Rate 5.5g/10min) was purchased from Arkema in pellet form and was used in the present study. The raw material pellets were dried in a vacuum chamber at 65°C for 4 hours before use. It consists of 80% hard segments of polyamide-12

(PA12) and 20% soft segments of poly(tetra-methylene oxide) (PTMO) by molecular weight [33]. According to literature [31, 39], the T_{mo} is 190°C and 184°C for PA12 and Pebax 7033 and the corresponding melting temperature of spherulite crystals T_{ms} is 176°C and 184°C, respectively. As discussed by Flory and Mandelkern [40], block copolymer melts at a temperature lower than the crystalline homopolymer, because of an effect associated with the presence of steric hindrances of the second component, which prevent the formation of perfect crystalline structures. Since Pebax 7233 has a slightly higher percentage of PA12 than 7033, its equilibrium melting temperature is expected to be between 184°C and 190°C and the melting temperature of spherulite crystals would be between 176°C and 184°C.

2.3 Experimental design

A two level half factorial design (2^{3-1}) was carried out to correlate process conditions with morphology development and mechanical properties, as arranged in Table 1. Each condition was replicated twice to evaluate statistical error regarding the effect of process on morphologies and mechanical properties. The single factorial experiments were followed to intuitively elaborate process-induced crystallization, in which mold temperature increases from 60 °C to 100°C, while injection velocity increased from 50 to 250mm/s. Barrel temperature was set as 210°C, 212°C, 207°C, 200°C, 45 °C from nozzle to barrel.

2.4 Sample preparation and characterization

Micro dumbbell specimens were cut into pieces and embedded into epoxy resin (Sigma Epoxy Embedding Medium kit 45359-1EA-F) and then cured at 45°C for 24 hours, followed by solidification at 60°C for another 24 hours. Samples were then trimmed and sectioned into 10µm thick slices by a Leica EM UC6 ultra-thin microtome using 45° glass knives. Procedure A (A cut) composed of cutting sections perpendicular to the flow direction in the ND-TD plane, as shown in Figure 4. B cut is assigned along the ND-FD plane. The cut slices were then sandwiched between two glass slides and observed under a Nikon Eclipse 80i

transmission Polarized Light Microscope (PLM). In addition, the remaining embedded blocks were sectioned and etched with 15% Trichloroacetic acid/H₂O (w/w) for 15 minutes^[41]. After cleaning with water and drying by hot air, the morphology of gold coated samples was then inspected with SEM.

Table 1. Experimental design

Run order	V _i (mm/s)	P _h (MPa)	T _m (°C)	ΔH _{c,PA12} (J/g)	Crystallinity
1	250	70	100	5.43	16.3
2	250	70	100	5.25	18.6
3	250	50	60	2.03	18.0
4	100	70	60	2.01	15.4
5	250	50	60	1.15	18.2
6	100	50	100	5.18	17.6
7	100	50	100	4.17	19.7
8	100	70	60	1.54	15.7

Note: V_i-Injection velocity, P_h-holding pressure, T_m-mold temperature

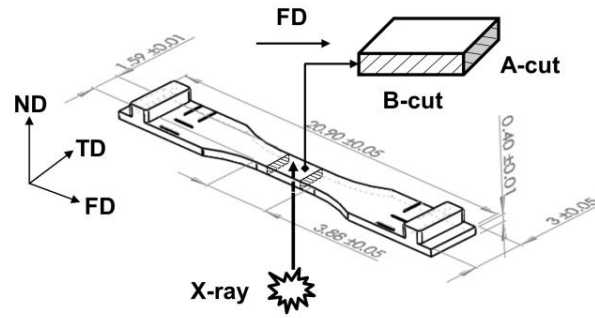


Figure 4. Sample sectioning (units: mm): A cut is along ND-TD plane, B cut is along ND-FD plane (ND, TD, and FD correspond to normal, transverse and flow direction).

Thermal analysis was carried out using a Mettler Toledo DSC 823e/500/670. The temperature profile consists of a heating stage followed by a cooling stage between -40°C and 220°C, at a rate of 10°C/min. The crystallinity of a copolymer is calculated as:

$$\begin{aligned} \%Crystallinity = & \left\{ x \times \frac{(\Delta H_{m,PA12} - \Delta H_{c,PA12})}{\Delta H_{PA12,100}} \times 100\% \right\} \\ & + \left\{ y \times \frac{(\Delta H_{m,PTMO} - \Delta H_{c,PTMO})}{\Delta H_{PTMO,100}} \times 100\% \right\} \end{aligned} \quad (4)$$

where x is the weight fraction of PA12, $\Delta H_{m,PA12}$ is the heat required to melt the crystals in the PA12 phase, $\Delta H_{c,PA12}$ is the enthalpy of the cold-crystallization in the polyamide phase, and $\Delta H_{PA12,100}$ is the theoretical heat of fusion for 100% crystalline PA12; y is the weight fraction of PTMO, $\Delta H_{m,PTMO}$ is the heat required to melt the crystals in the PTMO phase, $\Delta H_{c,PTMO}$ is the enthalpy of the cold-crystallization in the PTMO phase, and $\Delta H_{PTMO,100}$ is the theoretical heat of fusion for 100% crystalline PTMO. Weight fraction of PA12 was 0.8, determined elsewhere^[33], which is based on the ratio of PTMO and PA12. ΔH_m is a normalized enthalpy value calculated from the area of the melting peak, while $\Delta H_{100,PA12}$ is assumed to be 246J/g^[33]. Since no PTMO melting peak is observed around 7°C, the second term of Equation 4 is negligible.

Small/Wide angle X-ray Scattering (SWAXS) were carried out using an Anton Paar SAXSess instrument, operated at 40kV and 50mA with point collimation (beam size around $0.3 \times 0.2 \text{ mm}^2$) and finger-like beam stop. The distance between sample and detector was chosen as 261.2mm. The radiation used was a CuK α radiation with wavelength 0.154nm (PAN analytical X-ray source). Intensity profiles were recorded with a two-dimensional (2D) imaging plate. Scattering from oriented samples was radially averaging and was converted into a 1D profile in order to determine the angle of orientation and the degree of order. The scatter intensity was normalized by the primary beam in order to consider the sample absorption and eventual drift of the X-ray generator. The background under high vacuum conditions (0.1milli-Pa) was subtracted from the scattered intensity when calculating the orientation factor. The image contrast settings were kept the same with no treatment at evaluation. All the samples were exposed under X-ray for 1 hour in transmission mode though the thickness direction. The orientation of crystalline lamellae was quantified in the form of the Hermans orientation function from the 2D-SAXS scattering patterns, according to Equations 5 and 6^[42]:

$$f = \frac{3\langle \cos^2 \varphi \rangle - 1}{2} \quad (5)$$

$$\langle \cos^2 \varphi \rangle = \frac{\int_0^{\pi/2} I(\varphi) \cos^2 \varphi d\varphi}{\int_0^{\pi/2} I(\varphi) d\varphi} \quad (6)$$

where φ is the angle between the reference direction and normal direction of lamella. In the present case, the reference direction is defined to be the flow direction. If all the polymer chains are aligned parallel to the reference direction, f is 1. For an isotropic system f is 0. If the polymer chains lie in a plane perpendicular to the reference direction, f has the value of -1/2.

For oriented samples, a peak due to the structural periodicity was only found in the direction in which the sample is oriented. Long period L , representing the sum of average thicknesses of the crystal lamellae and the intermolecular amorphous regions, can be determined from the 1D scattering profiles:

$$L = \frac{2\pi}{q_{\max}} \quad (7)$$

where q_{\max} is the scattering vector at the maximum intensity. The contribution of the intensity of lamellae clusters of larger distances generates a more intense diffusion with small values of q , which influences the position of the maximum intensity. Lorentz correction is applied to amplify intensity and to refine the calculation of L , as shown in Equation 8:

$$I_c = I(q)q^2 \quad (8)$$

2.5 Mechanical properties

Uniaxial tensile testing was carried out to obtain bulk mechanical properties of micro dumbbell specimens. The large ridges of the samples were fitted into clamping slots on a specially designed holder in order to eliminate any slippage. The specimens were axially positioned in the middle of the clamp and screwed down. The pre-tightening force was then released before being tested under tension. The tensile speed was set as 5mm/s, according to

ASTM D638-03 for semi-rigid plastics. To get statistically reliable data, 5 tensile tests were carried out for each condition. Material mechanical properties were characterized by Young's modulus, tensile yield stress, yield strain, and nominal strain at break. Young's modulus was approximated by the secant modulus at 5% strain.

Nanoindentation was employed to study the local modulus and hardness of various morphological layers. Polymer samples were firstly embedded into epoxy resin and then solidified for more than 12 hours. The embedded samples were subsequently polished using silicon carbide paper (grade 2500), diamond suspensions ($3\mu\text{m}$) and colloidal silica (sub $0.05\mu\text{m}$). All experiments were performed at imposed depth of 500nm using a diamond Berkovich indenter tip using MTS Nanoindenter XP. Arrays of ~20 indentations were conducted across $400\mu\text{m}$ thickness at the ND-FD plane, as shown in Figure 4.

3. Results and discussion

3.1 Morphology observation

Pebax micro dumbbell parts exhibit a typical “skin-core” morphology, as shown by PLM and SEM in Figure 5. Such morphology is made up of four distinct layers: skin, fine-grained, oblate and core layers. The skin layer is composed of a thin fast solidification layer and a shear layer^[43]. The thin fast solidification layer is around $8\mu\text{m}$ thick, characterized as having no visible structure and appearing as a bright interference color due to birefringence, since the transcrystalline structure and/or heterogeneous nucleation of crystalline entities are too small to be visible under PLM^[21]. The shear layer is around $\sim 40\mu\text{m}$, which has been observed in neat PA6^[44]. A clear boundary exists between the shear layer and its adjacent fine-grained layer. The fine-grained layer has many fine spherulites beneath the skin layer, as shown in Figure 5 (a) and (b). The boundary between the fine-grained layer and the oblate spherulite layer is not as clear as that between the skin and the fine-grained layer. The oblate layer is composed of transition spherulites from the fine-spherulites to the large spherulites, and is characterized by a smaller external side adjacent to the fine-grained layer and a larger internal

side near the core. The core layer contains randomly large spherulites formed under quiescent-like conditions, where the cross-section of a spherulite resembles a polygon with diameter $\sim 10\mu\text{m}$. A $10\mu\text{m}$ thin slice sample microtomed (B cut) from a molded part was imaged using AFM under tapping mode. As shown in Figure 6, stacked layer-like structures are visibly aligned along the flow direction at the skin layer. Small spherulites of the fine-grained layer are $\sim 750\text{nm}$ in diameter, where a $1\text{-}2\mu\text{m}$ transition layer exists between the skin and the fine-grained layers. The oblate structure seems to be aligned along the thickness direction. Larger spherulite crystals are found at the core layer with similar dimensions measured from SEM and optical imaging. Using tapping mode of Atomic Force Microscope (AFM), a high phase angle region is featured as white color, corresponding to a stiffer area. The soft phase of PTMO in Pebax behaves as a soft rubber at ambient temperature, corresponding to a low phase angle region. The high phase angle region is actually complicated, and could be crystalline PA or glassy PA. However, no significant phase-separation morphology is observed in the AFM phase imaging. Additionally, some oriented-like structure beside the spherulites can be observed in Figure 6 (c), which could be due to scratches or deformations introduced to the sample during sectioning.

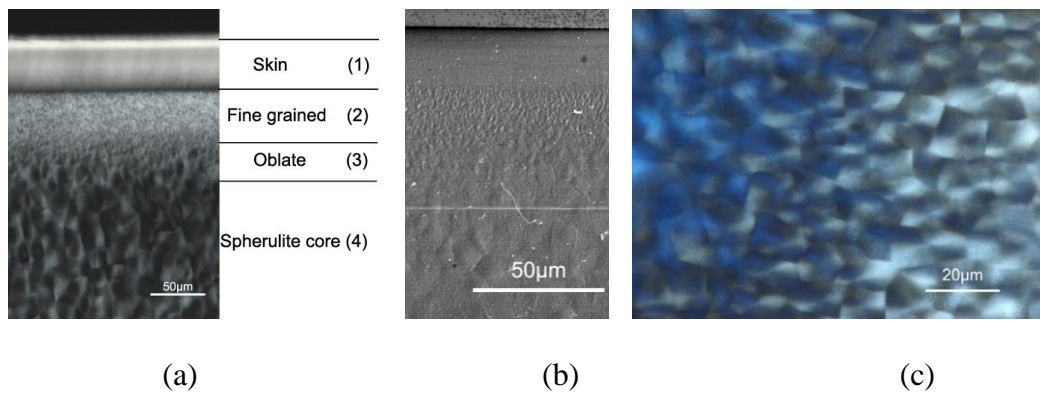


Figure 5. Morphology distribution of Pebax 7233: (a) morphological layers by PLM, (b) morphological layers by SEM, and (c) spherulite core.

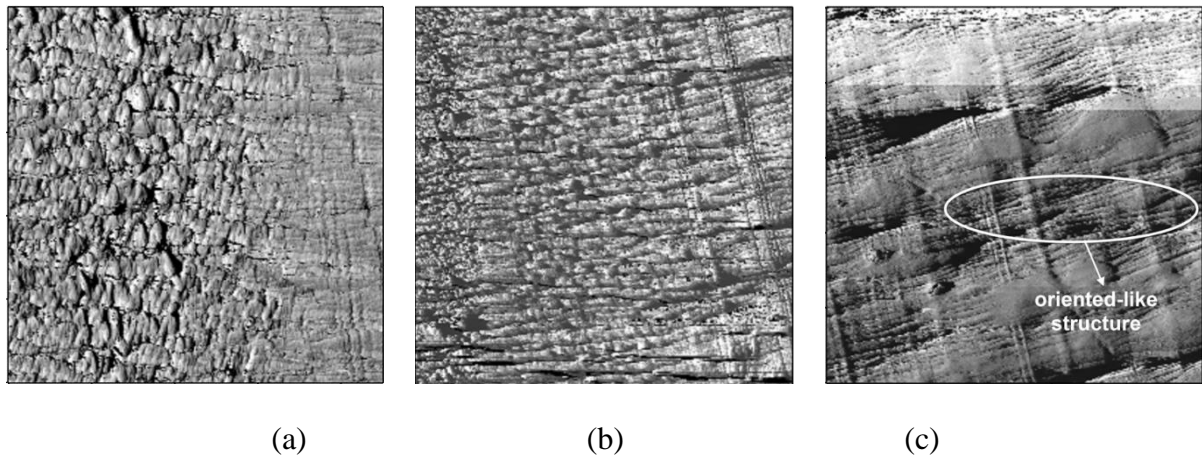


Figure 6. Tapping mode AFM phase images of morphology from skin to core (Note: skin to core is oriented from left to right; flow direction is assigned from bottom to top): (a) transition from skin to fine grained layer (scanning area: $9\mu\text{m}\times 9\mu\text{m}$), (b) transition from fine grained layer to oblate layer (scanning area: $40\mu\text{m}\times 40\mu\text{m}$), (c) spherulite core (scanning area: $50\mu\text{m}\times 50\mu\text{m}$).

3.2 Process-Morphology

3.2.1 Optical microscopy

Figure 7 shows the morphology variation under different process conditions. The average thickness of the morphological layers at the upper edge and the lower edge are displayed in Figure 8 (a). Cases 1 and 2 have the minimum skin thickness of $\sim 25\mu\text{m}$, while cases 4 and 8 have the maximum skin thickness of $\sim 65\mu\text{m}$. The skin layer of cases 3, 5, 6, and 7 have a similar medium thickness from $36\sim 43\mu\text{m}$. Statistical analysis in Figure 8 (b) implies that the skin layer is influenced by injection velocity and mold temperature, as reported for Polyoxymethylene (POM) ^[45, 46].

The fine-grained layer and oblate layer are much thinner than the skin layer and their thicknesses range from 6 to $13\mu\text{m}$. They are both absent for cases 3, 4, 5 and 8. As shown in Figure 8 (b), injection velocity and holding pressure both have a similar significant effect on the fine-grained layer, while holding pressure has a negligible effect on the skin layer. This indicates that nucleation of the fine-grained layer happens during the filling stage, while it

grows into small spherulites during the holding stage. Mold temperature has the most significant positive effect on the fine-grained layer. Jerschow et al. ^[11] described the fine grained layer as small spherulites without any orientation under PLM, which is formed at lower shear rates further from the mold wall. Once the shear stress is less than the critical shear stress, point nuclei would not grow into thread-like nuclei, but would instead grow into spherulitic crystals. It was reported by Schrauwen et al. ^[47] that the “shear layer” is created with thread-like nuclei and crystallizes in flow, while the “fine-grained layer” only nucleates in flow and crystallizes during the subsequent stages, as described in the present case.

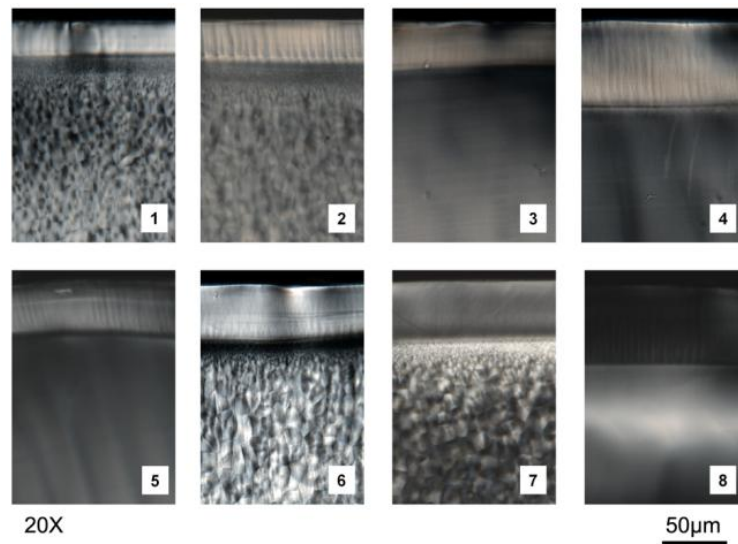


Figure 7. Variation of morphological layers (A cut) under various process conditions (c.f. Table 1).

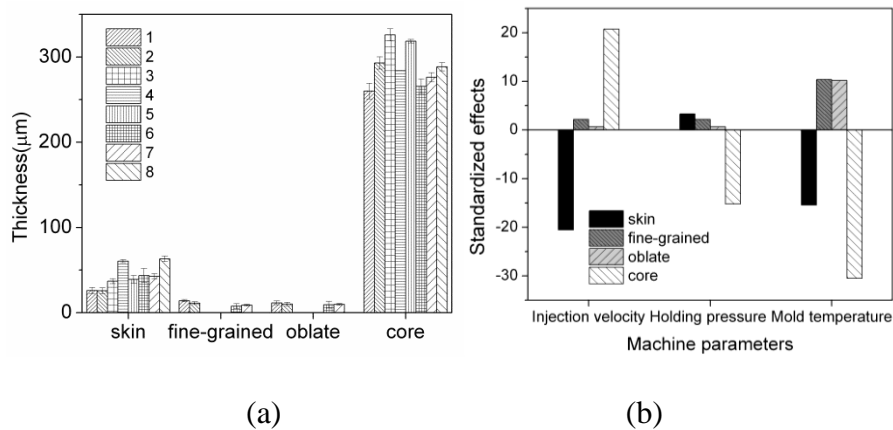


Figure 8. Morphology variation under different process condition: (a) thickness and (b) statistical analysis.

The thickness of the core layer ranges from 260~325 μm , and was solely determined by mold temperature. This means that the core layer was also formed in the cooling stage. In Figure 7, it is important to notice that we observed special spherulite-free core morphologies in cases 3, 4, 5 and 8, compared to the typical spherulitic core morphologies of case 1, 2, 6 and 7. Some core-free morphologies were found in micromolded parts of several materials, such as POM^[45] and HDPE^[25], where the core was either composed of oblate spherulite structures or an oriented row structure because of fast quench and high shear rates. For Pebax, microscopic observation reveals no perceptible structures in the central region. Under crossed polarized light, however, this region is gray, indicating that many tiny structures are actually formed. In addition, crystallinity measured by DSC does not change much for cases with spherulite-free cores, as shown in Table 1. Statistical analysis confirms that none of process parameters have a significant effect on crystallinity (see supporting information). Moreover, crystallinity increases slightly for cases 3 and 5, which have no spherulitic core region. This indicates that a core without large spherulites is composed of many small crystals, which are too small to be detected by polarized light microscopy. An explanation of the formation of such spherulite-free core structures is discussed below in Section 3.3.2.

One of the principal findings of this study is the appearance of irregular structures adjacent to the skin layer, marked by the red line box shown in Figure 9. For case 1, a ~30 μm thick layer with larger spherulites than those in the fine-grained layer is observed between the skin and fine-grained layer. The spherulites in this region undergo a transition from many fine ones to oblate spherulites, following the thermal gradients. Crystal size is similar to that in the oblate layer. A similar region, ~20 μm , can also be found for case 4. The crystals in this region are significantly larger than in its adjacent layers. The formation of such an irregular structure is because of a local temperature increase caused by shear heating. When a polymer melt passes down a flow channel, under the influence of a pressure drop Δp , if adiabatic conditions are assumed, the average temperature rise of the melt is^[48]:

$$\Delta T = \frac{\Delta P}{\rho c_p}$$

where the average cavity pressure drop Δp is ~ 21 MPa, melt density ρ is 0.8 g/cm^3 and polymer melt specific heat is $2800 \text{ J/kg}^\circ\text{C}$ at 210°C . The local temperature increase is $\sim 9^\circ\text{C}$. This temperature increase would reduce the effect of the thermal gradient and allow crystals to grow into a relatively larger size. Tan et al. ^[49] found that shear heating can cause the temperature to increase by $\sim 2^\circ\text{C}$ at the shear layer, compared to the core region, which changed the relaxation of fibers and influenced the final morphology. For the present case, high shear rates, up to $\sim 10^4 \text{ s}^{-1}$, could have accentuated this effect. However, such irregular microstructures do not present in every condition or even at different positions of a part, which depends strongly on local thermo-mechanical history.

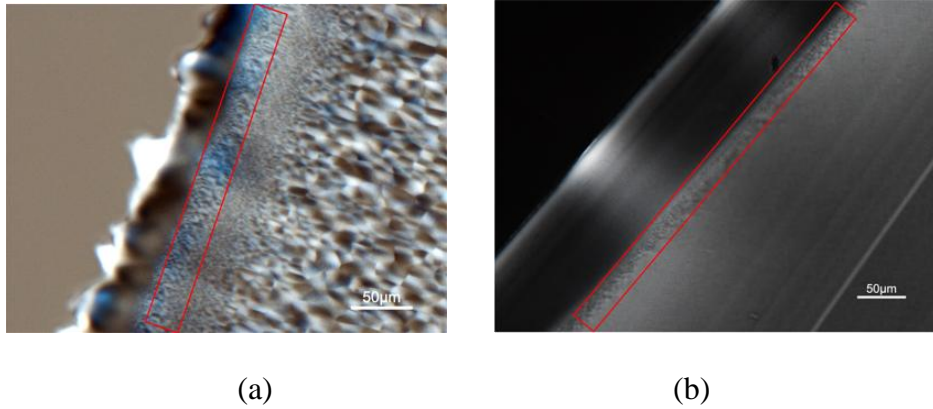


Figure 9. Irregular microstructure: (a) a large spherulite layer beneath the skin layer with a similar dimension of crystals in the oblate layer (case 1), (b) a spherulite layer between the skin layer and the spherulite-free core layer (case 4).

Two experiments had also been conducted based on the two most important factors, injection velocity ($50\sim 250 \text{ mm/s}$) and mold temperature ($60\sim 100^\circ\text{C}$), to confirm the above analysis and to identify the temperature range where a spherulite-free core forms; their morphology distributions are shown in Figure 10. A spherulite-free core structure is formed when mold temperature is within the range of $80\sim 90^\circ\text{C}$. The skin layer increases with injection velocity and decreases with mold temperature. The size of the fine-grained layer

increases with injection velocity and mold temperature. This is consistent with the statistical analysis. Furthermore, the crystallinity remains consistent regardless of the variation of injection velocity or mold temperature. This coincides with our statistical analysis and also indicates that the spherulite-free core region is composed of many small crystals.

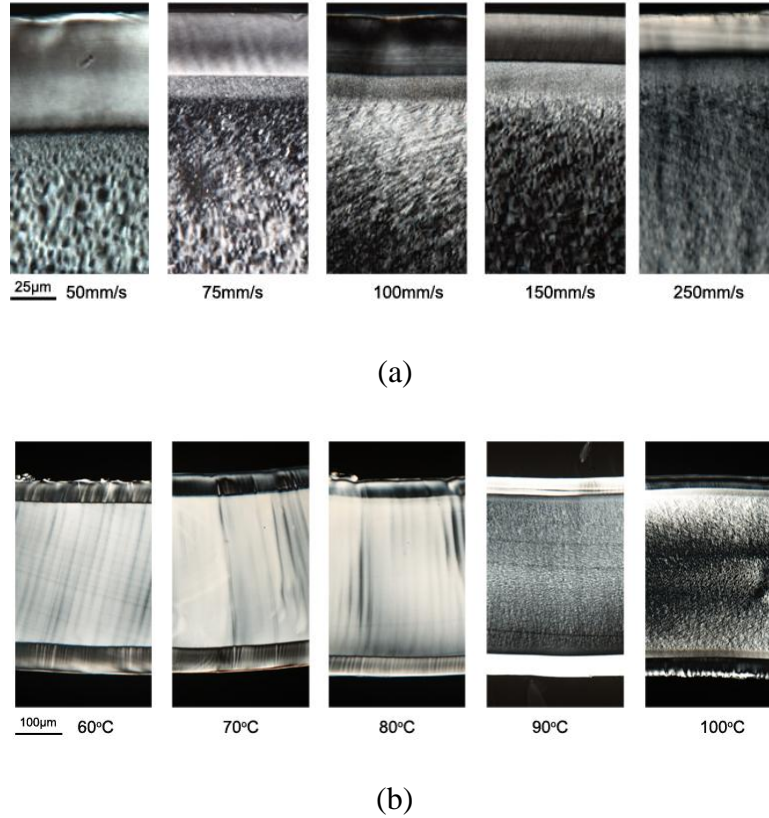
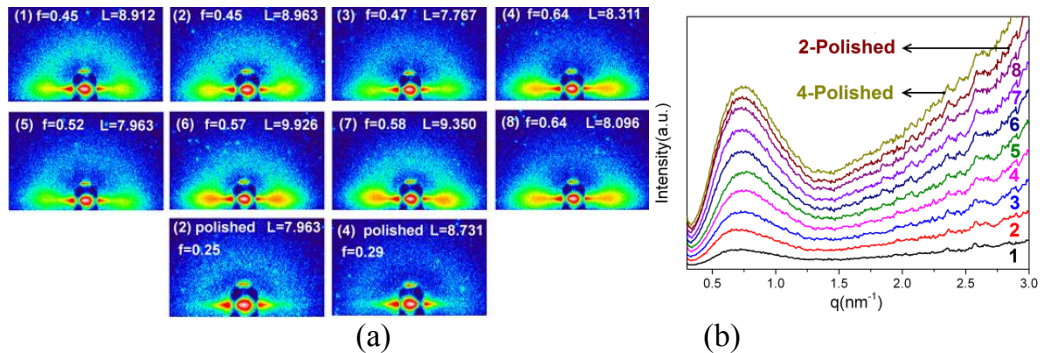


Figure 10. Morphology under various injection velocities (a) and mold temperatures (b).

3.2.2 Small and wide angle X-ray scattering (SWAXS)

As shown Figure 11 (a), Figure 12 (a) and (c), 2D scattering intensity is not evenly distributed and exhibits two most intensive regions at the meridian, indicating that all the samples are oriented. Cases 4 and 8 have the maximum orientation factors, 0.64, while cases 1 and 2 have the minimum values, 0.45. Statistical analysis, as shown in Figure 11 (c), implies that injection velocity and mold temperature are the most significant factors (negative) on the orientation factor. As indicated in Figure 12 (a), the lamella orientation factor decreases from 0.68 to 0.5, when injection velocity increases from 50mm/s to 250mm/s. For various mold temperatures, the orientation factor ranges from 0.54~0.6 and does not change significantly,

as indicated in Figure 12 (c). This is consistent with statistical analysis. It should be noticed that the overall molecular orientation does not increase with an increase of injection velocity. Instead, it depends on the thickness of oriented layers, when comparing Figure 10 (a) and Figure 12 (a). In Figure 12 (a), the intensity at the meridian reduces significantly, as indicated by the 2D scattering pattern after the skin was polished away. When the normalized orientation factor is correlated with the normalized skin layer thickness for all the experimental conditions, a roughly linear proportional relationship exists between them, as shown in Figure 13, which implies that the orientation is mainly generated from the skin layer, while the core layer is almost isotropic. Healy et al. ^[50] and Malhab & Regnier ^[51] examined molecular orientation of HDPE and found that increasing injection velocity and cavity thickness could decrease the level of orientation; however, neither of them were able to explain the reasons for this from a processing perspective. In a typical shish-kebab structure, two maxima were present at the equator and meridian in the 2D SAXS pattern, representing shish and kebab structure, respectively ^[52]. In the present study, only a meridional maximum is observed, which indicates that the oriented skin layer is mainly composed of stacks of oriented lamellae. Since the nucleation and growth of kebabs or lamellae perpendicular to the flow direction has to grow from shish or row nuclei, shish-like structures should be observed from the 2D SAXS pattern. The absent of an equatorial maximum is possibly because the size of the isolated shish structure is so small or the concentration of shish structure is too low to be detected by SAXS ^[52].



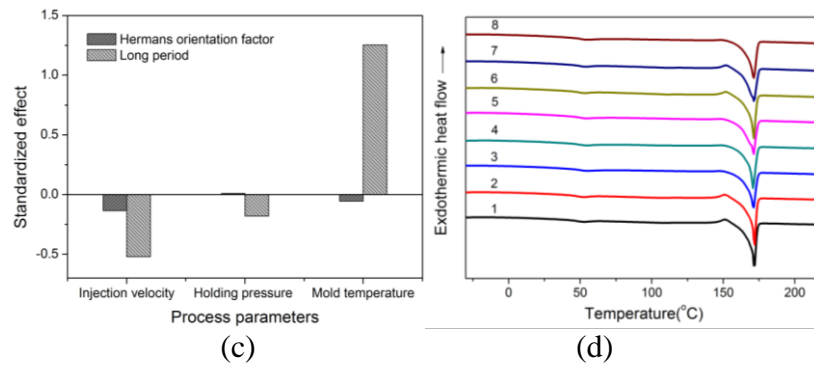


Figure 11. (a) 2D scattering patterns from case 1 to case 8 (flow direction is from left to right), (b) 1D normalized scattering intensity versus scattering vector from case 1 to case 8, (c) Statistical analysis, (d) DSC thermograph.

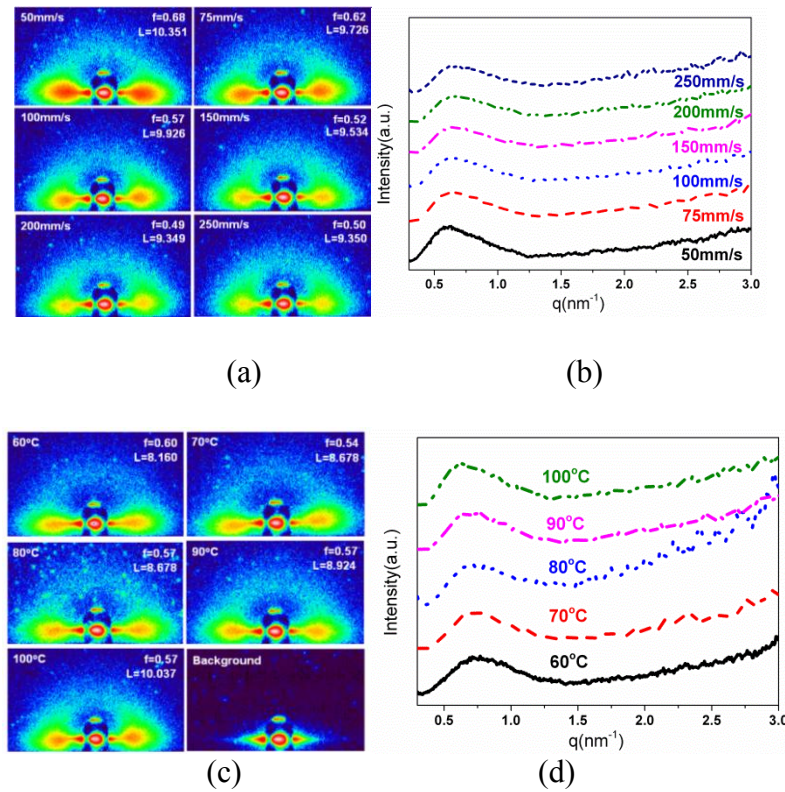


Figure 12. (a) 2D scattering patterns from 50~250mm/s (flow direction is from left to right), (b) Normalized scattering intensity versus scattering vector at various velocities, (c) Normalized scattering intensity versus scattering vector at various temperatures, (d) 2D scattering patterns from 60~100°C.

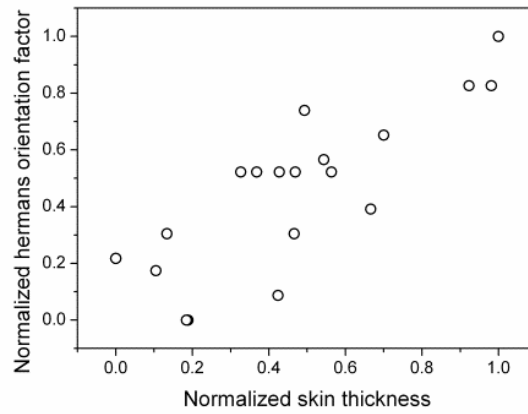


Figure 13. Relationship between overall orientation and skin thickness.

The long period of cases with a spherulite core (1 and 2, 6 and 8) is likely to be larger than cases with a spherulite-free core (3 and 5, 4 and 8), as indicated by Figure 11(b). Statistically, the average long period increases with mold temperature and decreases with injection velocity, as shown in Figure 11 (c). When injection velocity increases from 50mm/s to 250mm/s, the long period reduces from 10.35 to 9.35nm. Instead, when mold temperature increases from 60°C to 100°C, the long period increases from 8.16 to 10.04nm. Since lamella thickness is significantly affected by crystalline kinetics^[53], variation of injection velocity and mold temperature can influence the quench conditions and crystalline time, and thus affect the lamella thickness. However, explanation of this process effect needs careful study on the material crystallization process. When compared to compression molded Pebax 7033 thin films^[29], the long period of a micro molded part is 29%~47% narrower. In addition, the long period reduces from 8.963 to 7.963nm under case 2 after the skin layer is removed, indicating that the long period of the skin layer is possibly larger compared to the core layer. However, for case 4, no significant difference is observed from the 1D scattering curves before and after the skin layer has being removed.

It is also interesting to find an exothermal peak right before the endothermic peak from the DSC thermographs for cases 1, 2, 6, and 7, which have large spherulitic crystals, as shown in Figure 11 (d). This phenomenon resembles as cold crystallization, where an exothermic

peak occurred in between glass transition temperature and melting temperature during heating [54, 55]. The DSC plots for cases 1, 2, 6 and 7 seem similar to cases 3, 4, 5, and 8 apart from small peaks before large dips. Conditions with spherulite-free cores produced under high cooling rates seemed to minimize the magnitude of cold crystallization. A slower cooling enables nucleation and growth of large spherulite crystals, but some crystals are not perfect due to limited crystallization time and they could continue to crystallize until the proper crystallization temperature is reached. This behavior was also found by Rhee and White [56] for PA12 films during aging. The same behavior is also observed in cases with different injection velocities, all of which are associated with a large spherulitic core, as seen in Figure 14. This may be associated with the interfacial stress generated between metastable or imperfect crystal structure during formation upon cooling, in which the stress were then manifested as heat emitted when sufficient heat energy is supplied, enabling more flexible movement of polymer molecules, e.g. above glass transition temperature [55]. These exothermal peaks were also observed in cases where the mold temperature exceeds 90°C, allowing formation of a spherulitic core. The enthalpy of cold crystallization of PA12 is found directly proportional with mold temperature, suggesting higher amount metastable or imperfect crystals formed at lower cooling rate within Pebax (see supporting information Table S1).

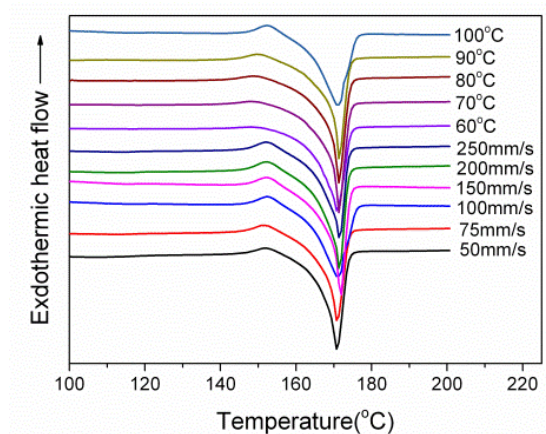


Figure 14. DSC thermographs showing endothermic peak in cold crystallization of PA12 at various velocities and mold temperatures.

In Figure 15, two main WAXS peaks are observed at $\sim 5.8^\circ$ and $\sim 21.5^\circ$, which correspond to the (001) and (020) diffraction planes of the γ phase of PA12, respectively^[57], as seen in Figure 15 (b). Another peak at $\sim 11.7^\circ$ presenting in configuration 2, when the sample is aligned vertically, is found to correspond to the (040) diffraction plane of the monoclinic γ phase, according to the crystal structure of PA12 proposed by Inoue and Hoshino^[56, 58]. As a result, the crystalline phase of Pebax 7233 SA01 can be deduced as being mainly the stable γ phase. Since the scattering intensity for the crystalline planes (001) and (020) at the meridian diminishes after the skin layer is polished away, crystals in the core layer are much less oriented or more isotropic, as indicated in Figure 15 (c). This is further supported by decreased hermans orientation factor after the skin removal, see Figure 11 (a).

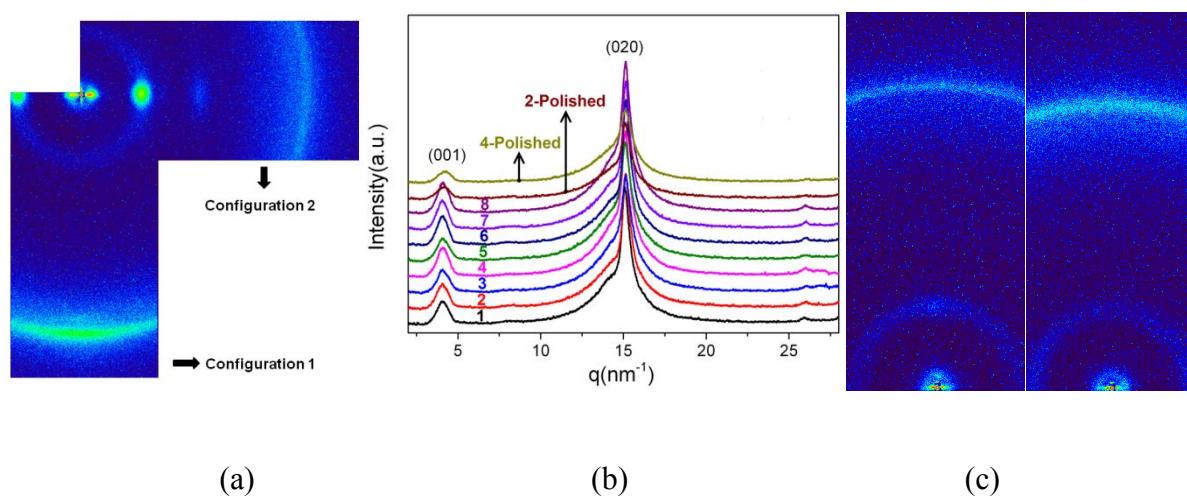


Figure 15. (a) 2D scattering patterns of configuration 1 (sample aligned along FD) and configuration 2 (sample aligned perpendicular to FD), (b) 1D intensity profile of configuration 1, (c) 2D scattering of case 2 (left) and 4 (right) after skin layer being polished away.

3.3 Morphology interpretation

3.3.1 Flow induced crystallization

As discussed in the introduction section, injection molding is a short term shear protocol under high stress and high shear rates with non-isothermal conditions and thermomechanical history. In the present work, the shear stress varies from 0.3MPa to 0.6MPa with shear time ranging from 0.007s to 0.0042s over various conditions, which are around 1 and 2~3 orders of magnitudes higher than in a laboratory based short-term shear protocol, respectively. Due to the difficulties of resolving birefringence and/or X-ray scattering on the msec time scale, and the difficulties of implementing well-defined conditions for a short-term shear protocol in an industrial process, it is not possible to study flow-induced crystallisation in injection molding using a laboratory based method.

Relying on the fact that shear stress in pressure driven flow varies linearly along the channel thickness direction from zero at the center line to the maximum at the wall ^[14, 15] (see Figure 16), we used in-line process monitoring and morphology observation to study flow induced crystallization in injection molding process. The linear profile of shear stress is derived directly from a force balance, which is independent of the material's viscoelastic properties in the channel and velocity boundary conditions in the wall ^[15]. The flow is considered to be fully developed with no viscoelastic flow present in the region between sensor 1 and sensor 2, as indicated by morphology observations ^[59]. Process parameters in the plastisization stage are maintained constant the same for all process conditions to ensure the polymer melt has a general uniform thermomechanical history before injection.

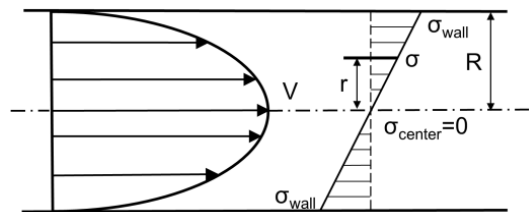


Figure 16. Schematic of velocity profile and shear stress profile across the gap of the rectangular slit channel.

As justified by Mykhaylyk et al.'s SAXS study ^[1] and real time depth section used by Kornfield et al. ^[15], morphology transition can be detected by PLM. Since wall shear stress can be calculated from Equation 3, the corresponding critical shear stress at the morphology interface can be estimated from:

$$\frac{\sigma}{\sigma_{wall}} = \frac{r}{R} \quad (9)$$

where σ is wall shear stress, σ_{wall} is the critical stress at the morphology interface, r and R are distances from the center of the cavity to the morphology interface and to the cavity wall, respectively, see Figure 16. Because the skin layer develops during non-isothermal filling, the effective flow width decreases during filling and this will influence the measurement of shear stress, which will be discussed later in this section.

The specific work (SP), w , is defined by Janeschitz-Kriegl ^[6] as the work done on a unit volume of sheared polymer melt:

$$w = \int_0^{t_s} \eta[\dot{\gamma}(t)] \dot{\gamma}^2(t) dt \quad (10)$$

where η is the shear rate dependent viscosity, $\dot{\gamma}(t)$ is shear rate and the integration is over the entire shearing time, t_s . Because obtaining the shear rate in a pressure driven flow is complicated by material properties, only the apparent specific work at the wall can be estimated:

$$w = \bar{\eta} \dot{\gamma}^2 t_s \quad (11)$$

where $\bar{\eta}$ is the average viscosity over the experienced apparent shear rates, t_s is the shear time, which is estimated by the cavity filling time (Δt_f) when polymer melts travel from sensor 1 to sensor 2 (see Figure 3). In the present work, flow condition is characterized by wall shear stress and apparent wall specific work.

In conditions where the injection velocity increases from 50mm/s to 250mm/s at the same degree of supercooling (70°C), the specific work ranges from 95~126MPa and has a

similar pattern to the wall shear stress when the shear rate increases, as shown in Figure 17 (a).

The maximum specific work is achieved by the lowest shear rate; the minimum specific work occurs between 10000s^{-1} and 15000s^{-1} , which is because of the interactions between the shear rate, shear time and viscosity. As indicated in Figure 17 (a), the critical shear stress for forming the skin and fine-grained layers are consistent, almost independent of the shear rates. The critical shear stress to form the skin layer is 0.3MPa with a standard deviation of 0.016 , when the shear rate increases from $4\times 10^3\text{s}^{-1}$ to $2.5\times 10^4\text{s}^{-1}$. The critical stress for forming the fine-grained layer is 0.27MPa with a standard deviation of 0.013 . The degree of supercooling is defined as a temperature difference between the equilibrium melting temperature ($\sim 184^\circ\text{C}$) and the mold interface temperature ^[31]. Figure 17 (b) shows that the skin thickness increases as the degree of supercooling increases, while the fine-grained layer reduces with an increase of the degree of supercooling. Generally, the higher the degree of supercooling, the faster the solid-liquid interface advances into the core of the sample, which creates a thicker skin. A thicker skin acts as a heat more efficient isolator and gives rise to a thinner fine-grained layer. The average specific work also increases directly with the degree of supercooling, but the critical shear stresses of the skin layer and the fine-grained layers do not change with the degree of supercooling. They remain consistently at 0.26MPa with a standard deviation of 0.006 , which approximates the critical stress under various shear rates. As a result, we can conclude that shear stress is independent of skin thickness and processing conditions for the same part. This proves that shear stress is a good threshold to characterize the onset of an oriented structure under any real injection molding process. This may enable control of morphology and even properties by monitoring and controlling shear stress.

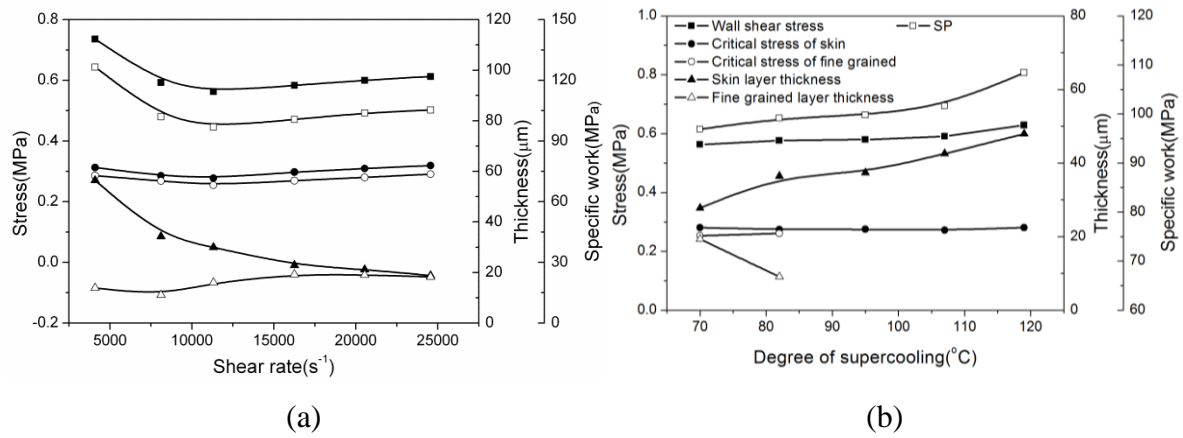


Figure 17. Variation of critical stress, morphology thickness and specific work (SP) with (a) shear rate, (b) degree of supercooling.

However, critical shear stress is not the same for all the conditions and it has standard deviations ranging from 0.006 to 0.013. Such deviation suggests how better to define a threshold value for the onset of oriented structures. Figure 18 shows the variation of critical shear stress of the skin layer with degrees of supercooling and shear rates. Obviously, with respect to all the molding conditions, critical shear stress remains consistent over a wide range of the degree of supercooling for a narrow range of shear rates. This implies that quenching alone has a minor effect on the formation of oriented structures. However, if the degree of supercooling remains constant, the critical shear stress presents a pattern of first increasing and then decreasing when shear rate increases. Since the critical shear stress is calculated from the skin layer thickness and wall shear stress, it is reasonable to claim that heat transfer can significantly reduce the effective thickness of a flow channel at lower shear rates, leading to an increased flow resistance and consequently to increased shear stresses. At the same time, high-speed injection needs a high driving force, which results in an increased wall shear stress and critical shear stress.

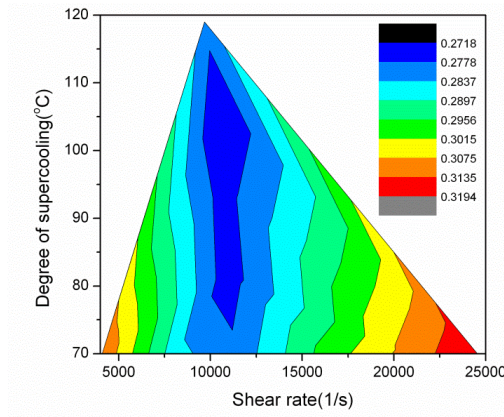


Figure 18. Distribution of critical shear stress for the onset of oriented structures against shear rates and degree of supercooling at a fixed cavity thickness 400 μ m.

Since both quench and specific work can promote nucleation, it would be interesting to see the interaction of both on skin layer development, as mapped in Figure 19. Skin ratio is found to increase with specific work at a lower degree of supercooling (high mold temperatures). This effect gets weaker when the degree of supercooling increases. Nevertheless, the maximum skin ratio can only be achieved at the highest specific works and low to medium degrees of supercooling. This further explains the role of flow on the formation of oriented structures. It is also interesting that skin ratio does not directly increase with the degree of supercooling, when the specific work is constant. Crystallisation from thermal and flow effects determine the skin layer thickness and final part anisotropy.

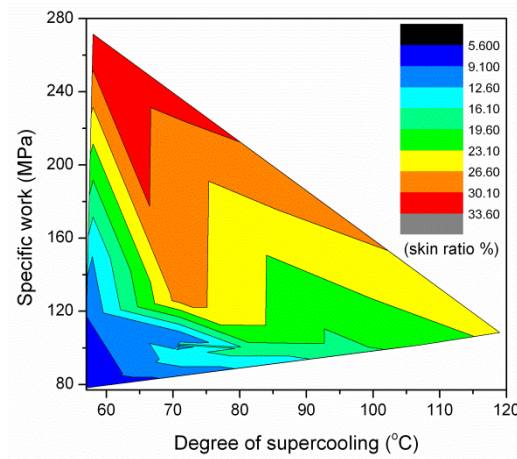


Figure 19. 2D mapping of skin ratio versus specific work and degree of supercooling.

3.3.2 Formation of spherulite-free core structure

When the degree of supercooling is greater than 90°C with a corresponding molding temperature below 80°C, the central region of the part ends up with a spherulitic-free structure. The white interference color indicates that a variety of tiny crystals occupy the central region. Temperature-Time-Transformation curves (TTT curves) are used to explain crystallization kinetics of slow crystallizing polymers, such as PA12, Poly(phenylene sulfide), Poly(ether-ether-setone) and Syndiotactic polystyrene^[39, 60], which have been applied for the first time to Pebax 7233 in the present work. The schematic of the TTT curves in Figure 20 illustrates the locus of points at which crystallization begins versus temperature and logarithmic time. If the melt cooling curves intersect the TTT curves, crystallization starts. Otherwise, the polymer melt is supercooled to form a glassy-like structure. Furthermore, stress induced orientation and stretching can enhance the crystallization rate and shifts the TTT curves to the left and upwards^[61]. Each stress level corresponds to one TTT curve. Here, we relate the critical shear stress of different morphological layers to these critical TTT curves in order to explain the formation of spatial structures. The boundary mold temperatures leading to a spherulite core structure are in the range of 80~90°C. It is known that the cooling rate is higher near the surface and is lower near the core. As shown in Figure 20 (a), both cooling curves of location A at $T_m=80^\circ\text{C}$ and 90°C intersect the curve of the wall shear stress, σ_{wall} , but do not crossover the curve of the critical stress of the skin, σ_{skin} , implying the formation of a skin layer. At location B, the cooling curve of $T_m=90^\circ\text{C}$ intersects the curve of the critical stress of the skin layer, but not the curve at the critical stress of the fine grained layer, $\sigma_{\text{fine-grained}}$, which leads to the creation of a fine-grained layer, while the cooling rate at $T_m=80^\circ\text{C}$ is too fast to intersect any TTT curve, leading to a glassy-like structure. In addition, because the shear stress at location B at $T_m=80^\circ\text{C}$ is still less than the critical stress of the skin layer, many nuclei grow into many small crystals because of high quench and yet they are too small to be detected by PLM, forming so-called “glassy-like structure” in the present work. At location C, the cooling

curve at $T_m=90^\circ\text{C}$ crosses both TTT curves at the critical stress of the fine-grained and the core layers, implying that an oblate transcrystalline layer and a core layer finally form, along with a skin and a fine grained layer. However, the cooling rate at $T_m=80^\circ\text{C}$ is still too high to form a spherulitic core.

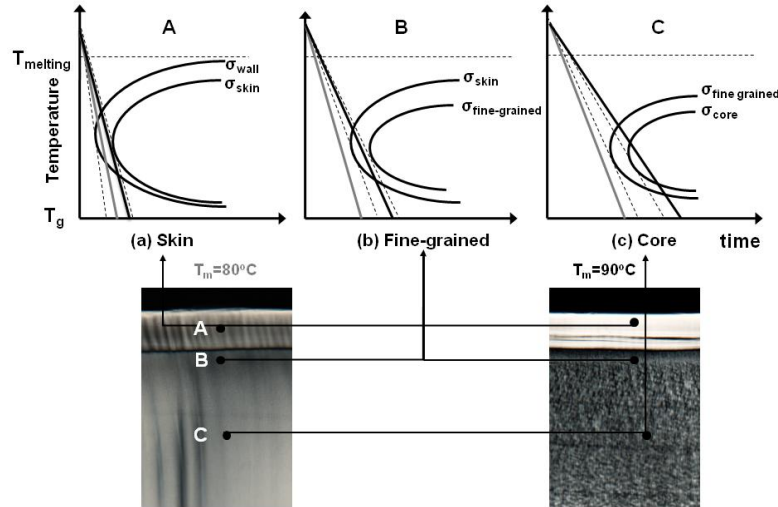


Figure 20. TTT diagrams for the development of morphology layers (dotted line is the critical TTT curve; big black dot on crystalline image is the corresponding position; cooling rate is marked by gray line ($T_m=80^\circ\text{C}$) and black line ($T_m=90^\circ\text{C}$)).

3.4 Mechanical properties

The engineering stress-strain curves of microinjection molded Pebax parts were obtained from uniaxial tensile tests at various process conditions and given in Figure 21. Mechanical properties of micro parts and standard tensile specimens (from material supplier) are compared, as listed in Table 2. Although processing methods would affect mechanical properties, this comparison would still indicate how much difference exists between macro samples and micro samples. Young's modulus under micro molding is approximately half of that for a conventional macroscale specimen; strain at break is 30% less than expected from material supplier data sheets; yield stress and yield strain are 1.6~2 times higher than standard samples. The following section attempts to explain this discrepancy from a processing perspective.

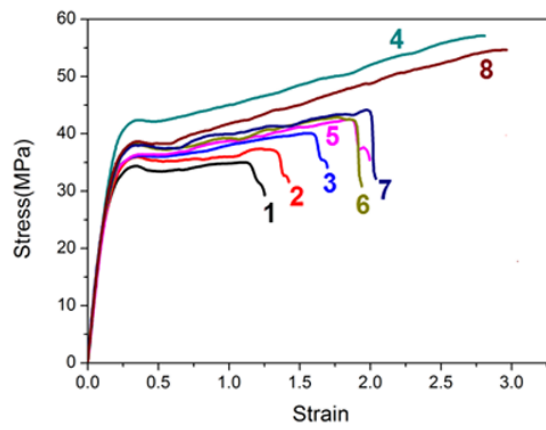


Figure 21. Macroscopic tensile behavior of microinjection molded samples at various process conditions.

Table 2. Comparison of Pebax 7233 mechanical properties (maximum) under two typical morphologies with data of standard specimens from material supplier (n=5 for present listed experiments).

	Young's Modulus (MPa)	Strain at break (%)	Yield stress (MPa)	Yield strain (%)
μ IM(spherulitic core)	275	204	39	35
μ IM (non-spherulitic core)	263	269	42	37
Arkema(ISO 527-1/-2)	522	>300	26	18

3.4.1 Nanoindentation

The distribution of hardness and modulus of the skin, fine-grained, oblate and core layers are studied using nanoindentation along the thickness direction at the ND-FD plane, as shown in Figure 22. The modulus first decreases from the skin to the fine-grained, oblate layer and then increases at the core layer. This distribution is non-symmetric because of the non-uniform mold temperature of the moving half and stationary half. The moduli of the skin and core layer under process condition 5 (spherulite-free core) are 0.85 ± 0.06 GPa and 0.78 ± 0.11 GPa, respectively. For condition 6 (spherulite core), they are 0.96 ± 0.16 GPa and 0.83 ± 0.04 MPa.

This indicates the that skin layer has a higher modulus than the core layer for Pebax, regardless of the core structure, as similar observation was reported in polypropylene [62]. Indentation hardness measures the resistance of a material to local deformation produced on a surface by a sharp indenter upon application of a given load [63]. For polymer material, hardness is related to crystallinity, glass transition temperature and crystal thickness, etc. The hardness of skin and core layer under process condition 5 is $0.075\pm0.008\text{GPa}$ and $0.068\pm0.014\text{GPa}$, respectively. Under process condition 6, the hardnesses of the skin and core are $0.083\pm0.009\text{GPa}$ and $0.071\pm0.003\text{GPa}$, respectively. Hardness and modulus of an injection molded part are affected mainly by crystallinity and superstructure, such as cross-hatched lamellae [17]. It was reported that crystallinity decreased from the core to the surface for both microinjection molding [25] and conventional injection molding [10], because of quenching at the mold wall. Therefore, the higher modulus and hardness at the skin layer is mainly attributed to its highly oriented structure [17].

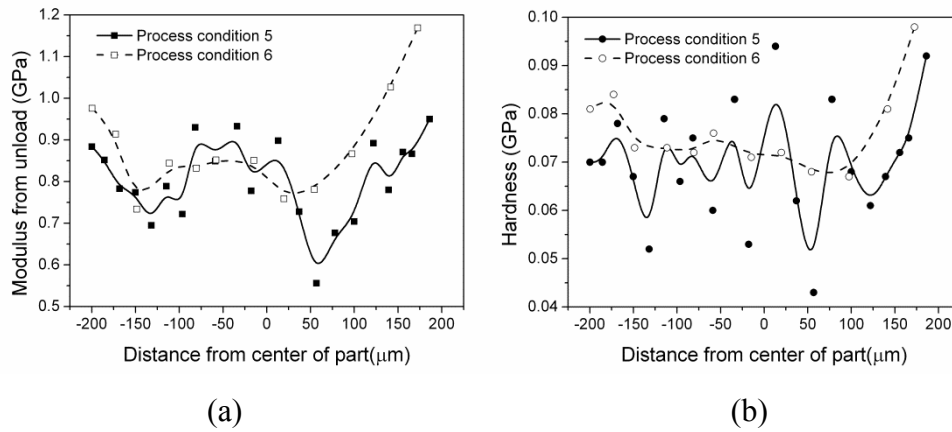
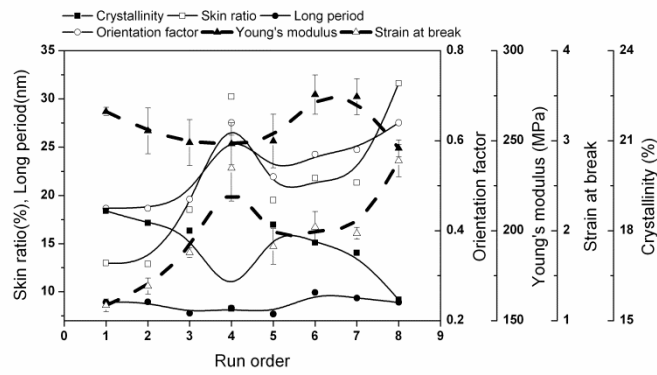


Figure 22. Modulus and hardness distribution across thickness direction for case 5 (spherulite-free core) and case 6 (spherulite core): (a) indentation modulus, (b) hardness.

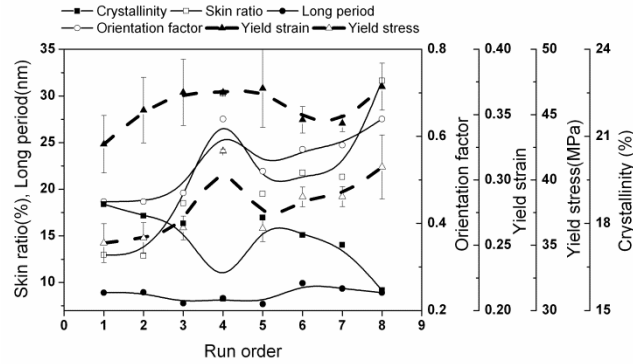
3.4.2 Bulk mechanical properties

Figure 23 shows the variation of Young's modulus, strain at break, yield stress, and yield strain of samples produced under each process condition (see supporting information Table S1). Skin ratio and orientation factor exhibit similar patterns, since the overall molecular

orientation is influenced mainly by the thickness of the oriented skin, as indicated previously in Figure 13. The crystallinity has exactly the opposite pattern to the skin ratio, which implies that the skin layer has a lower crystallinity than the core layer. The long period changes in a narrow range and does not follow the variation of skin ratio. Strain at break follows the patterns of skin ratio and molecular orientation, which indicates that a thicker skin gives rise to higher elongation. Statistical analysis in Figure 24 shows that the strain at break increases with a decrease of injection velocity and mold temperature, since they reduce the skin thickness. When mold temperature increases from 60°C to 100°C, strain at break decreases with an increase of mold temperature, following the trend of the skin ratio, as shown in Figure 25 (a), regardless of core structures. Meanwhile, in Figure 26 (a), when injection velocity increases from 50mm/s to 250mm/s, strain at break increases with an increase of skin ratio and orientation factor, while crystallinity and long period have little variation. But this result contradicts previous studies, where the skin layer was found to be easy to fracture because of oriented structures ^[64, 65]. Fujiyama et al. ^[66] reported that the skin layer had a higher yield point and ruptured without necking; high yield was explained as being due to fibril structures, which had high strength; rupture without necking was because kebabs were aligned perpendicular to the uniaxial tensile direction, and rotation of these about the tensile direction was difficult and thus unfolding of molecular chains was also difficult. Such a discrepancy may be because the crystallinity of the skin is lower than in the core, which contains more amorphous soft segment PTMO and amorphous hard segment PA12. The soft segment of Pebax (PTMO) could work as a rubber-like connection between the amorphous phase and crystalline phase, meaning that lamella rotation and unfolding would occur earlier. In addition, skin has a lower concentration shish structure, which facilitates lamella orientation and unfolding.

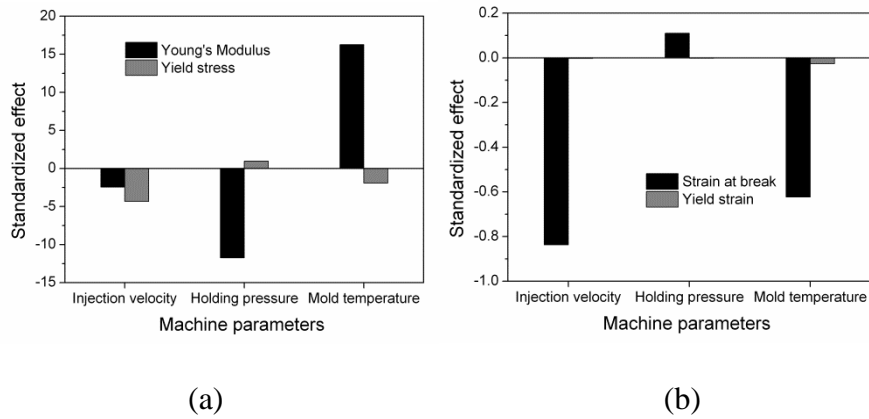


(a)



(b)

Figure 23. Variation of morphology (crystallinity, skin ratio, long period, and orientation) and mechanical properties: (a) Young's modulus and strain at breaks, (b) yield stress and yield strain.



(a)

(b)

Figure 24. Statistical analysis of effect of process parameters on mechanical properties: (a) Young's modulus, strain at break; (b) yield stress and yield strain.

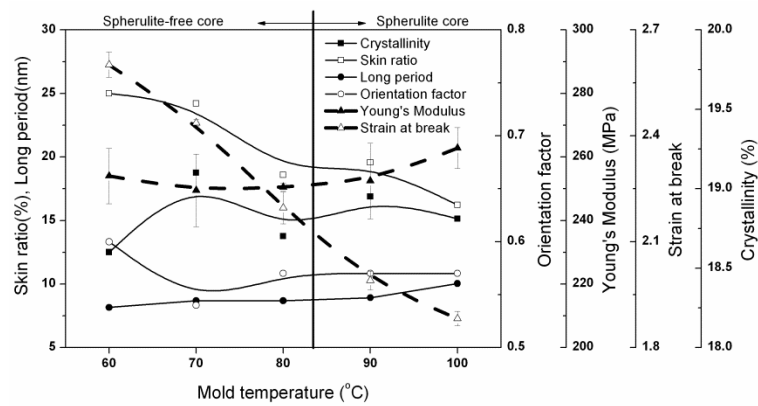
Young's modulus of Pebax samples produced under different processing conditions exhibits a complex pattern, where cases of spherulite cores (cases 1, 2, 6 and 7) have a higher modulus than cases of spherulite-free core (cases 3, 4, 5 and 8), as shown in Figure 23 (a). When mold temperature increases from 60°C to 80°C (corresponding to spherulite-free core), the modulus decreases slightly, and then increases when mold temperature rises from 80°C to 100°C (corresponding to spherulitic core). For Pebax, deformation under low strain is confined to the soft segment PTMO and amorphous hard segment PA12. Spherulite crystals can serve as rigid “fillers” to reinforce the softer matrix and enhance the modulus by an increase in the spherulite concentration ^[67]. Modulus decreases with a decrease of skin ratio and orientation factor, when injection velocity increases from 50 to 250mm/s, as seen in Figure 26 (a). In accordance to nanoindentation test results, indentation modulus and hardness of the core are slightly lower than of the skin. The skin is composed of oriented lamellae. At lower strain, the soft segment is gradually aligned by affine deformation along the uniaxial tension direction and lamella rotate with their long axes orientated towards the tension direction ^[30]. Such rotation is difficult because the oriented lamellae and shish structures are restrained, resulting in a high modulus. Since the skin behaves stiffer than the core, its relative importance on the global properties of an injection molded part is then enhanced by the thickness of the skin.

Yield stress follows the same varying patterns of the skin ratio and orientation factor with the degree of crystallinity, as shown in Figure 23 (b). Statistically, yield stress increases with a decrease of injection velocity and mold temperature, as shown in Figure 24. When mold temperature increases from 60°C to 100°C, the yield stress decreases first for the spherulite-free core as there is a decrease of skin ratio, and then increases for the spherulitic core, as shown in Figure 25 (b). In addition, in Figure 26 (b), yield stress decreases with a decrease of skin ratio and molecular orientation, as the injection velocity increases from 50mm/s to 250mm/s. The high yield stress of the skin layer is considered to be due to shish

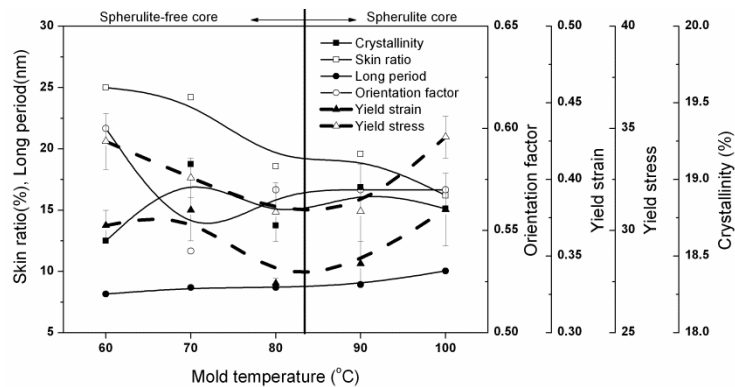
structures, because fibrous crystals have a high strength and deeply penetrated texture [66].

Although shish structures are not detected by SAXS, they still exist and would consequently enhance yield stress. Oriented lamellae of the skin can also resist stress in the tension direction and can contribute to a higher yield stress.

Yield strain weekly follows the variation of skin ratio and orientation factor, which is the opposite for the crystallinity. Statistical analysis confirms that yield strain increases with a decrease of mold temperature, as shown in Figure 24. It is also seen that cases 1, 2, 6, and 7 have a lower yield strain than cases 3, 4, 5, and 8, which indicates that spherulite-free cores are associated with a higher yield strain. As shown in Figure 25 (b), yield strain first increases and then decreases, and finally increases when the core structure changes to spherulite crystals. Additionally, yield strain increases with an increase of injection velocity, which follows the opposite trend of skin ratio and molecular orientation, as shown in Figure 26 (b).



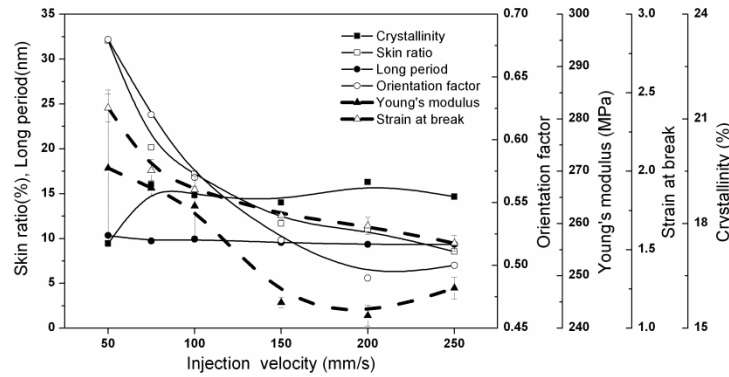
(a)



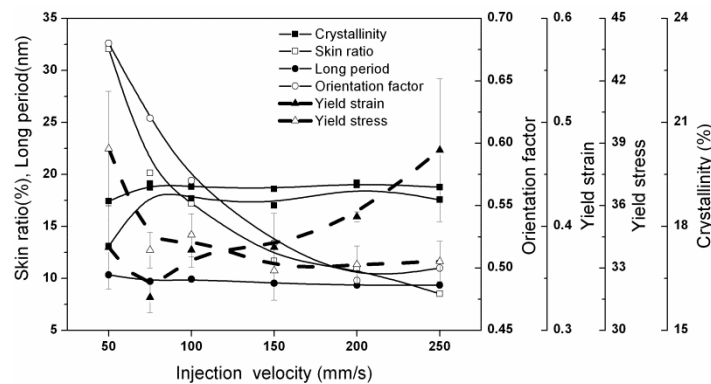
(b)

Figure 25. Effect of mold temperature on morphology and mechanical properties: (a)

Young's modulus, strain at break; (b) yield stress and yield strain.



(a)



(b)

Figure 26. Effect of injection velocity on mechanical properties: (a) Young's modulus and Strain at break, (b) yield stress and yield strain.

4. Conclusions

In the present work, crystallization of Pebax 7233 micro dumbbell part under the microinjection molding process and its effect on mechanical properties have been studied. Firstly, a typical “skin-core” morphology is found in Pebax samples with two types of core structures: large spherulitic cores and spherulite-free cores, depending on quench conditions, which is explained by reference to TTT diagram. The stable γ phase of PA12 is the main crystallization phase of Pebax 7233, as discovered by WAXS. Process conditions that lead to spherulitic cores exhibit significant cold crystallization behavior unlike those of spherulite-

1 free cores. Secondly, the thickness of the skin layer is determined by injection velocity and
2 mold temperature; the fine-grained layer is influenced by injection velocity, holding pressure
3 and mold temperature; the oblate and core layers are determined by mold temperature.
4 Irregular “large spherulite” structures form beneath the skin layer because of local shear
5 heating. Molecular orientation of micromolded parts is governed by the thickness of the
6 oriented layer.
7
8
9
10
11
12
13

14 Nanoindentation indicates that the skin layer has a higher modulus and hardness than the
15 core, regardless of the core structures (spherulitic or non-spherulitic). Bulk mechanical
16 properties are closely related to skin-core morphology: strain at break and Young’s modulus
17 both increase with an increase of skin-ratio and orientation; yield stress also increases with an
18 increase of skin ratio, but yield strain decreases with an increase of skin ratio, provided that
19 the core has the same structure. High shear rates and thermal gradients of microinjection
20 moldings influence crystallization kinetics and modify skin ratio and induce variation in
21 crystallinity, molecular orientation, and crystal length etc., all of which influence mechanical
22 properties and differ significantly from macro sized samples. Mechanical testing at the micro
23 scale is necessary in order to understand material behavior at this level.
24
25
26
27
28
29
30
31
32
33
34
35
36
37
38

39 A comparison method between a “short-term shear protocol” and microinjection molding
40 was proposed so as to prove that a threshold for the onset of oriented structures in a laboratory
41 based process is still valid for the high stress, high shear rates associated with real processing
42 conditions. It was found that the critical shear stress at the skin layer is 0.298MPa with
43 standard deviation 0.024, which is almost independent of flow conditions. Shear stress proved
44 to be a good candidate to characterize the onset of oriented structures under real molding
45 conditions. This means that using shear stress as an in-line feedback signal during processing
46 may enable in-line control of product morphology and thus product properties.
47
48
49
50
51
52
53
54
55
56
57
58
59
60
61
62
63
64
65

Acknowledgements: The authors gratefully acknowledge financial support from Enterprise Ireland (Grant Nos. CFTD/07/314, CF/2012/2022) and European Regional Development Fund. We also acknowledge Dr. Brian Rodriguez and Miss Denise Denning for help with AFM imaging. We also appreciate the assistance of Mrs. Tiina O'Neill and Prof. Dimitri Scholz for training on microtome and polarized light microscopy. Special thanks also go to Dr. Wilhelm Risse for his kind help with DSC.

Keywords: shear induced crystallization, short-term shear protocol, spherulite-free core structure, critical shear stress, specific work

Reference:

- [1] O. O. Mykhaylyk, P. Chambon, C. Impradice, J. P. A. Fairclough, N. J. Terrill, A. J. Ryan, *Macromolecules* **2010**, *43*, 2389.
- [2] G. Kumaraswamy, R. K. Verma, A. M. Issaian, P. Wang, J. A. Kornfield, F. Yeh, B. S. Hsiao, R. H. Olley, *Polymer* **2000**, *41*, 8931.
- [3] D. W. T. Lucia Fernandez-Ballester, and Julia A. Kornfield, *Journal of Rheology* **2009**, *53*, 1229.
- [4] E. G. Liedauer s, Janeschitz-Kriegl H, Jerschow P, Geymayer W, Ingolic E, *International polymer processing* **1993**, *3*, 236.
- [5] J. S. Tiang, "Shear induced crystallization of nucleated polymers", in *Department of Chemical Engineering*, McGill University, Montreal, Quebec, Canada, 2010, p. PhD/.
- [6] H. Janeschitz-Kriegl, E. Ratajski, M. Stadlbauer, *Rheol Acta* **2003**, *42*, 355.
- [7] O. O. Mykhaylyk, P. Chambon, R. S. Graham, J. P. A. Fairclough, P. D. Olmsted, A. J. Ryan, *Macromolecules* **2008**, *41*, 1901.
- [8] L. Fernandez-Ballester, D. W. Thurman, W. Zhou, J. A. Kornfield, *Macromolecules* **2012**, *45*, 6557.
- [9] G. Kumaraswamy, R. K. Verma, J. A. Kornfield, *Review of scientific instruments* **1999**, *70*, 2097.
- [10] J.-W. Housmans, M. Gahleitner, G. W. M. Peters, H. E. H. Meijer, *Polymer* **2009**, *50*, 2304.
- [11] P. Jerschow, H. Janeschitz-Kriegl, *Rheol Acta* **1996**, *35*, 127.
- [12] H. Janeschitz-Kriegl, "Crystallization modalities in polymer melt processing: fundamental aspects of structure formation", Springer, Wien New York, 2010.
- [13] H. Janeschitz-Kriegl, E. Ratajski, *Colloid Polym Sci* **2010**, *288*, 1525.
- [14] Z. Ma, L. Fernandez-Ballester, D. Cavallo, T. Gough, G. W. M. Peters, *Macromolecules* **2013**, *46*, 2671.
- [15] L. Fernandez-Ballester, D. W. Thurman, J. A. Kornfield, *Journal of Rheology* **2009**, *53*, 1229.
- [16] J. S. Tiang, J. M. Dealy, *Polymer Engineering & Science* **2012**, *52*, 835.
- [17] M. van Drongelen, T. B. van Erp, G. W. M. Peters, *Polymer* **2012**, *53*, 4758.

- [18] N. Zhang, J. S. Chu, C. J. Byrne, D. J. Browne, M. D. Gilchrist, *Journal of Micromechanics and Microengineering* **2012**, 22, 065019.
- [19] B. R. Whiteside, M. T. Martyn, P. D. Coates, P. S. Allan, P. R. Hornsby, G. Greenway, *Plastics, Rubber and Composites* **2003**, 32, 231.
- [20] F. Liu, C. Guo, X. Wu, X. Qian, H. Liu, J. Zhang, *Polymers for Advanced Technologies* **2012**, 23, 686.
- [21] G. Julien, C. Thierry, M. Patrice, *Journal of Micromechanics and Microengineering* **2009**, 19, 025023.
- [22] C. Guo, F. H. Liu, X. Wu, H. Liu, J. Zhang, *Journal of Applied Polymer Science* **2012**, 126, 452.
- [23] A. Jungmeier, G. W. Ehrenstein, D. Drummer, *Plastics, Rubber and Composites* **2010**, 39, 308.
- [24] C. Yang, *The International Journal of Advanced Manufacturing Technology* **2013**, 1.
- [25] J. Giboz, A. B. Spoelstra, G. Portale, T. Copponnex, H. E. H. Meijer, G. W. M. Peters, P. Mélé, *Journal of Polymer Science Part B: Polymer Physics* **2011**, 49, 1470.
- [26] E. Haberstroh, M. Brandt, *Macromolecular Materials and Engineering* **2002**, 287, 881.
- [27] A. L. Kelly, T. Gough, B. R. Whiteside, P. D. Coates, *Journal of Applied Polymer Science* **2009**, 114, 864.
- [28] N. Zhang, M. D. Gilchrist, *Polymer Testing* **2012**, 31, 748.
- [29] J. P. Sheth, J. Xu, G. L. Wilkes, *Polymer* **2003**, 44, 743.
- [30] Y. Song, H. Yamamoto, N. Nemoto, *Macromolecules* **2004**, 37, 6219.
- [31] B. Tavernier, J. Mewis, P. Van Puyvelde, M. Takenaka, B. Ernst, T. Hashimoto, *Polymer Engineering & Science* **2008**, 48, 2418.
- [32] D. A. Mair, E. Geiger, A. P. Pisano, J. M. J. Frechet, F. Svec, *Lab on a Chip* **2006**, 6, 1346.
- [33] S. Armstrong, B. Freeman, A. Hiltner, E. Baer, *Polymer* **2012**, 53, 1383.
- [34] B. B. Sauer, R. S. McLean, R. R. Thomas, *Polymer International* **2000**, 49, 449.
- [35] B. B. Sauer, R. S. McLean, D. J. Brill, D. J. Londono, *Journal of Polymer Science Part B: Polymer Physics* **2002**, 40, 1727.
- [36] C. Rean-Der, J. Wen-Ren, C. Shia-Chung, *Journal of Micromechanics and Microengineering* **2005**, 15, 1389.
- [37] H. M. Laun, *Rheol Acta* **1983**, 22, 171.
- [38] N. Zhang, M. D. Gilchrist, *Polymer Engineering & Science* **2013**, DOI: 10.1002/pen.23677.
- [39] C. J. G. Plummer, J. E. Zanetto, P. E. Bourban, J. A. E. Månson, *Colloid Polym Sci* **2001**, 279, 312.
- [40] P. J. Flory, L. Mandelkern, *Journal of Polymer Science* **1956**, 21, 345.
- [41] G.-S. Yang, F.-C. Lu, *Acta Polymerica Sinica* **1992**, 6, 708.
- [42] U. Göschel, *Polymer* **1995**, 36, 1157.
- [43] V. Tan, M. R. Kamal, *Journal of Applied Polymer Science* **1978**, 22, 2341.
- [44] B. Yalcin, M. Cakmak, *Polymer* **2004**, 45, 2691.
- [45] M. R. Kamal, J. Chu, S. Derdouri, A. Hrymak, *Plastics, Rubber and Composites* **2010**, 39, 332.
- [46] E. S. Clark, *Applied Polymer Symposium* **1973**, 20, 325.
- [47] B. A. G. Schrauwen, L. C. A. v. Breemen, A. B. Spoelstra, L. E. Govaert, G. W. M. Peters, H. E. H. Meijer, *Macromolecules* **2004**, 37, 8618.
- [48] N. Mills, *"Plastics: Microstructure and Engineering Applications"*, Elsevier Science, 2005.
- [49] L. P. Tan, S. C. Joshi, C. Y. Yue, Y. C. Lam, X. Hu, K. C. Tam, *Acta Materialia* **2003**, 51, 6269.
- [50] J. Healy, G. H. Edward, R. B. Knott, *Journal of Applied Crystallography* **2007**, 40, s393.

- [51] N. B. Malhab, G. Regnier, *AIP Conference Proceedings* **2011**, 1353, 820.
- [52] P.-w. Zhu, G. Edward, *Polymer* **2004**, 45, 2603.
- [53] A. Romankiewicz, T. Sterzynski, *Macromolecular Symposia* **2002**, 180, 241.
- [54] R. M. R. Wellen, M. S. Rabello, *Journal of Materials Science* **2005**, 40, 6099.
- [55] J. F. Mano, Y. Wang, J. C. Viana, Z. Denchev, M. J. Oliveira, *Macromolecular Materials and Engineering* **2004**, 289, 910.
- [56] S. Rhee, J. L. White, *Polymer Engineering & Science* **2002**, 42, 134.
- [57] L. Bai, Z. Hong, D. Wang, J. Li, X. Wang, G. Pan, L. Li, X. Li, *Polymer* **2010**, 51, 5604.
- [58] K. Inoue, S. Hoshino, *Journal of Polymer Science: Polymer Physics Edition* **1973**, 11, 1077.
- [59] N. Zhang, "Characterization of micro injection molding process for replication of micro/nano scale features and micro components", in *School of mechanical and materials engineering*, University College Dublin, Dublin, 2013, p. Doctor of Philosophy/244.
- [60] M. C. a. B.Yalcin, "Evolution of structural hierarchy in injection molded semicrystalline polymers", in *Injection molding: technology and fundamentals*, A.I.I. M. R. Kamal, S. Liu, Ed., Hanser, Munich, 2009.
- [61] C.-M. Hsiung, M. Cakmak, J. L. White, *Polymer Engineering & Science* **1990**, 30, 967.
- [62] Z. Lu, K. F. Zhang, *The International Journal of Advanced Manufacturing Technology* **2009**, 40, 490.
- [63] G. G. H. Michler, F. J. B. Calleja, *Mechanical Properties Of Polymers Based On Nano-Structure And Morphology*, Taylor & Francis Group, 2005.
- [64] J. C. Viana, A. M. Cunha, N. Billon, *Journal of Materials Science* **2001**, 36, 4411.
- [65] S. Meister, D. Drummer, *Polymer Testing* **2013**, 32, 432.
- [66] M. Fujiyama, T. Wakino, Y. Kawasaki, *Journal of Applied Polymer Science* **1988**, 35, 29.
- [67] Y. Mohajer, G. L. Wilkes, *Journal of Polymer Science: Polymer Physics Edition* **1982**, 20, 457.

Support Information

[Click here to download Production Data: Support information.docx](#)